Bioprinting 11 (2018) e00034

Contents lists available at ScienceDirect

Bioprinting

journal homepage: www.elsevier.com/locate/bprint

Towards preserving post-printing cell viability and improving the resolution: Past, present, and future of 3D bioprinting theory

Eric Lepowsky[a], Metin Muradoglu[b], Savas Tasoglu[a,c,d,e,f,*]

[a] Department of Mechanical Engineering, University of Connecticut, Storrs, CT 06269, USA
[b] Department of Mechanical Engineering, Koc University, Sariyer, Istanbul, Turkey
[c] Department of Biomedical Engineering, University of Connecticut, Storrs, CT 06269, USA
[d] Institute of Materials Science, University of Connecticut, Storrs, CT 06269, USA
[e] Institute for Collaboration on Health, Intervention, and Policy, University of Connecticut, Storrs, CT 06269, USA
[f] The Connecticut Institute for the Brain and Cognitive Sciences, University of Connecticut, 337 Mansfield Rd, Storrs, CT 06269, USA

ARTICLE INFO

Keywords:
Bioprinting
Post-printing viability
Bioprinting theory
Bioprinting computational modeling

ABSTRACT

Three-dimensional bioprinting as an additive manufacturing technology for constructing biomimetic tissues by the deposition of individual layers is an ever growing and evolving field. Bioprinting has found many applications across tissue engineering and regenerative medicine disciplines, including medical research, regenerating human tissues for transplantation, and conducting stem cell research. In order to maintain the forward momentum of bioprinting, it is necessary to consider major factors limiting bioprinting's capabilities: post-printing cell viability and printing resolution. Computational modeling has the capacity to investigate the impact dynamics of encapsulated cells as they are deposited, with a particular focus on determining the deformation of the encapsulated cell and the rate of deformation, which are dependent on, among other factors, viscoelastic features, droplet size, and velocity. Similarly, computational models can be utilized to optimize filament integrity in extrusion-based bioprinting. By harnessing the power of modeling, experimental parameters can be predicted and fine-tuned to improve cell viability and/or shape fidelity. Herein, we review extrusion-based, droplet-based, and laser-based bioprinting techniques. The respective computational models are then presented, including compound droplet impact models for droplet-based bioprinting, which incorporated a Newtonian-model and viscoelastic features, and computational models applied to extrusion-based bioprinting. We then conclude with the future direction of bioprinting theory.

1. Introduction

Three-dimensional (3D) bioprinting is an advancing technology for the fabrication of biomimetic tissues and organs. Bioprinting, in essence, is an additive manufacturing method whereby complex, functional living 3D structures are formed by depositing progressive layers of cell-laden bioinks. The need for precise, on-demand, and high-throughput production of cell-laden structures bolsters bioprinting's growing importance and relevance. This need for bioprinting is supported by the several emerging application fields within tissue engineering and regenerative medicine [1], including: organ-on-a-chip for medical research [2–4]; replicating diseased tissues, such as tumor-on-a-chip, for investigating the process of diseases [5–8]; regenerating human tissues, such as skin, cartilage, and bone, for transplantation [9–12]; and conducting stem-cell research [13]. As the field of bioprinting continues to grow, progress must look towards remedying the limiting factors of bioprinting, such as preserving post-printing cell viability and improving the resolution of printing techniques.

Modeling offers a way to investigate the impact dynamics of encapsulated cells as they are deposited [14,15]. Modeling of the bioprinting process can be grouped according to deposition principles or actuation principles. Firstly, deposition principles encompass the form in which material is deposited, such as droplet-based or extrusion-based printing [15]. For instance, modeling of droplet-based deposition would consider the impact of the droplets and printed constructs, while modeling of extrusion would look at the point in time when constructs are created to the point when they are deposited. Secondly, actuation principles include the specific manner by which the deposited material is formed. Taking droplet-based deposition as an example, possible actuation principles include piezoelectric or thermal inkjet printing, among other techniques, for which modeling would focus on the pressure wave's or vapor bubble's effect on the liquid

* Corresponding author at: Department of Mechanical Engineering, University of Connecticut, Storrs, CT 06269, USA.
E-mail address: savas.tasoglu@uconn.edu (S. Tasoglu).

https://doi.org/10.1016/j.bprint.2018.e00034
Received 13 July 2018; Received in revised form 24 September 2018; Accepted 28 September 2018

steam, respectively. Similarly, for laser-based deposition, modeling may look at the actuation principle of laser-induced thermal effect on gel substrates. In general, when modeling the bioprinting process, the cells and the cell-encapsulating liquid – together, these form the bioink– are each treated as a fluid [15]. For instance, the modeling of droplets may consider an inner droplet representing a cell, an encapsulating droplet, and the ambient fluid. In order to predict the effect of the bioprinting process on cells, cell viability is considered to be a function of various characteristics of the encapsulated cell [14]. Bioprinting simulations are performed for a range of parameters to determine the deformation/elongation of the encapsulated cell and the rate of deformation with respect to droplet-size and velocity, both of which are theorized to be related to cell damage.

Herein, we begin with a review of the existing technologies for 3D bioprinting. The technologies described are categorized by deposition principles into extrusion-based, droplet-based, and laser-based printing techniques. We then discuss the corresponding computational models for these techniques. For droplet-based bioprinting, compound droplet impact models are covered, including a Newtonian model and a discussion of viscoelastic features. A future perspective is also offered for using such modeling to enable informed decision making in regards to setting experimental parameters. Computational models are then discussed for application to extrusion-based bioprinting. Finally, we conclude with a look towards the future of 3D bioprinting theory.

2. 3D bioprinting technologies

There are several technologies and methods that have been demonstrated for 3D bioprinting, which may be categorized into extrusion-, droplet-, and laser-based printing techniques [16,17]. Each technique utilizes a different overarching printing scheme. Extrusion-based techniques print with a continuous stream of material. Droplet-based techniques deposit material in the form of individual drops, which commonly results in higher resolution than extrusion. Laser-based printing, which is also a high-resolution technique, uses a laser to deposit cell-laden material onto a receiving substrate or consists of a reservoir of material that is cured or solidified by some form of a laser. Herein, we detail the unique features of each individual technology within these categories.

2.1. Extrusion-based printing techniques

Extrusion-based printing is a very common technique within the field of 3D printing which entails extruding, or forcing, a continuous stream of melted solid material or viscous liquid through a sort of orifice, often a nozzle or syringe (Fig. 1). Specifically, for bioprinting, extrusion-based techniques are limited to those compatible with aqueous hydrogel materials since the process of heating the material, as required for solid materials, is damaging to hydrogels and reduces biocompatibility [18–20]. Such techniques include 3D plotting, direct ink writing, and pressure-assisted micro-syringe. There are also additional techniques which have not been directly applied for bioprinting but do promise biological applications, such as low-temperature deposition and robocasting.

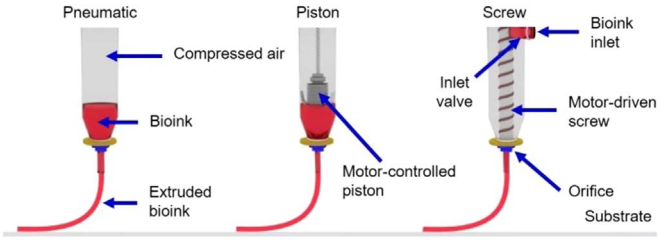

Fig. 1. Extrusion-based printing techniques [6]. Extrusion-based techniques, in general terms, are pneumatic-, piston-, or screw-driven. Pneumatic extrusion uses compressed air to force bioink through the nozzle's orifice. Piston extrusion utilizes a motor-controlled piston to apply mechanical force to extrude the bioink. Screw extrusion has an inlet for bioink which is drawn through nozzle by a screw positioned down the middle of the nozzle. For all types, the bioink is extruded as a continuous stream. Reproduced, with permission, from [6].

2.1.1. 3D plotting

A basic extrusion-based printing technique is 3D plotting, which is compatible with a variety of biocompatible materials, including hydrogels, nanocomposites, polymers, and biologics such as proteins, growth factors, or cells [21–24]. 3D plotting utilizes a syringe with a micro-sized needle through which loaded material is extruded [25]. Using a stepper motor or a pneumatic valve for volume- or pressure-driven extrusion, respectively, the material loaded into the syringe is dispensed as a micro-strand. The thickness of the micro-stand is dependent on various parameters, including the viscosity of the printing material, the rate of extrusion, and the diameter of the needle. 3D plotting has been demonstrated for tissue engineering scaffolds by plotting directly into a liquid solution of similar density to that of the printed material [25]. The printed material is cured by a reactive substance included in the liquid solution, or by using a mixing nozzle which combines the printing material with an initiator during printing.

2.1.2. Direct ink writing

Similar to 3D plotting, direct ink writing, or direct write assembly, is a straightforward pneumatic extrusion printing technique whereby hydrogels are forced through a cylindrical nozzle and orifice by compressed air [26]. In direct ink writing, the hydrogel is deposited onto a stage in such a way that the hydrogel is either pre-cured or cures upon deposition. To improve the structural integrity of the printed structures, hydrogels must include a larger proportion of solids, such as nanoparticles or colloidal networks [27].

2.1.3. Pressure-assisted micro-syringe

The pressure-assisted micro-syringe technique uses compressed air and a pneumatically-driven micro-syringe for hydrogel microfabrication. The micro-syringe is typically constructed from a steel syringe, which offers temperature control of the material, and a glass capillary needle, which enables small feature size [28–30]. This micro-syringe is affixed to a computerized, three-axis micro-positioner which allows for precise positioning, coupled with the precise deposition provided by the micro-syringe [28]. For the purpose of fabricating hydrogel structures without living cells, a solution can be made of the desired printing material and a volatile solvent; however, for printing with cells, a different biocompatible curing method would need to be implemented.

2.1.4. Additional techniques

Low-temperature deposition implements a screw-style nozzle by which solidified hydrogels are able to be printed. Since the hydrogel is not subjected to any heating process, heat related degradation is avoided [31]. However, since the nozzle deposits the solid hydrogel onto a sub-zero degree (freezing) platform, this process is not compatible with printing live cells. Low-temperature deposition is more well-suited for printing scaffolds, material sans living cells, by freeze drying to remove any remaining water-based solvent from the solidified hydrogel, thereby yielding a semi-rigid structure. Multiple nozzles can be combined to enable gradients and more complex structures [32].

Another technique that is indirectly related to bioprinting for scaffold fabrication is robocasting. Robocasting uses a nozzle-equipped dispensing head to extrude a slurry mixture from a syringe to a movable platform [33]. Traditionally, robocasting has been applied for manufacturing ceramic scaffolds by printing with hydrogels highly loaded with ceramic powder. After printing, the hydrogel would then be burned out, resulting in a ceramic structure that could be sintered into a rigid form. Although ceramics are not pertinent to bioprinting, the

robocasting process shows potential for fabricating hydrogel-based composites for various applications, including hydrogels loaded with cells, growth factors, or other biological substances. As compared to 3D plotting or direct ink writing which extrude cured or nearly-cured material, robocasting is compatible with non-cured hydrogel materials and introduces the concept of forming hydrogel composites by mixing other substances into the hydrogel. Additionally, robocasting refers exclusively to a moving extruder, whereas comparable techniques may utilize a moving extruder and/or a moving platform.

2.2. Droplet-based printing techniques

As opposed to the continuous stream of material that is printed in extrusion-based printing, droplet-based printing techniques deposit individual, discrete drops of material [34]. Droplet-based techniques offer relatively high resolution, as compared to extrusion, attributed to the small volume deposited at a time. There are several droplet-based techniques including acoustic droplet ejection, pressure-assisted micro-valve bioprinting, and inkjet bioprinting [16]. Inkjet bioprinting follows the same concept as traditional inkjet printing on paper and can be further classified into continuous inkjet printing and drop-on-demand printing, the latter of which is more favorable owing to its economical operation, facile control, and ability to produce complex or multi-material patterns [32]. Drop-on-demand inkjet printing techniques described below include thermal, piezoelectric, electrostatic, and electrohydrodynamic jetting. Additionally, inkjet printing can be applied to binder deposition.

2.2.1. Acoustic droplet ejection

Acoustic droplet ejection utilizes an acoustic field to eject droplets from an open pool of printing material [35]. An acoustic bioprinter consists of two-dimensional microfluidic channels in which the bioink is contained. The bioink at the very small opening of the channels has sufficient surface tension to prevent the bioink from spilling out. A piezoelectric substrate with gold rings generates acoustic waves on demand; the produced waves are circular and converge to a focal point at the interface between the bioink and air at the channel exit. Droplets are formed when the force exerted by the acoustic waves exceeds to the surface tension [35,36]. Acoustic bioprinting is advantageous since the bioink, along with any constituent living cells, are not exposed to heat, high pressure, significant voltages, or large shear stress during droplet ejection, all of which are common stressors in droplet-based printing techniques. However, acoustic bioprinting has drawbacks: the gentle forces that acoustic fields produce may not be sufficient for forming droplets of viscous bioinks (i.e. hydrogel with high cell concentration) and the apparatus is prone to excessive droplet ejection due to external disturbances.

2.2.2. Pressure-assisted micro-valve bioprinting

A micro-valve bioprinter consists of a pressurized reservoir of liquid bioink and a nozzle with an electromechanical micro-valve controlled orifice (Fig. 2A) [37–39]. Most typically, the micro-valve dispensing head is constituted by a solenoid coil and a plunger which blocks the orifice when in its resting position [16]. When voltage is applied to the solenoid, a magnetic field is produced which pulls the plunger upwards, unblocking the orifice in the nozzle. While the nozzle is open, if the back pressure in the reservoir is sufficiently large to overcome the surface tension at the orifice, the pressure forces the bioink through the orifice. The pressure and the valve-gating time then collectively cause the plunger to drop, sealing off the orifice, thereby forming a droplet. By controlling the pressure, orifice geometry, bioink rheological properties, and, when applicable, cell concentration, the droplet volume and cell viability can be manipulated [40].

2.2.3. Continuous inkjet bioprinting

Continuous inkjet bioprinting refers to the manner of producing the droplets: droplets are formed continuously, but the printing material is still ejected in discrete droplets. The material is pneumatically forced through a nozzle and then broken up into continuous droplets by leveraging Rayleigh-Plateau instability [41]. Rayleigh-Plateau instability results in a phenomenon by which a cylindrical volume of liquid jet is perturbed by the potential energy of the surface energy of the jet and the kinetic energy of the motion of the jet [16,42]. The perturbation grows exponentially when the wavelength of the perturbed jet exceeds its initial radius such that the product of the wave number and the initial jet radius is less than one [16]. Eventually, the jet of bioink distorts to minimize its potential energy, thereby breaking into a continuous stream of droplets, not to be confused with the unbroken stream of material seen in extrusion-based printing (Fig. 2C).

2.2.4. Thermal inkjet bioprinting

Thermal inkjet printing is a drop-on-demand inkjet printing technique that employs a thermal element within the print head to generate droplets of the bioink (Fig. 2D). The heating element is electrically controlled to produce cyclic spikes in thermal energy [43]. The thermal energy is transferred to the bioink causing partial vaporization, forming a small bubble, thereby providing a small pulse of pressure to force the bioink out of the nozzle as the bubble collapses [1,44]. The elevated heating temperature is typically within the range of 200–300 °C. Despite the high temperatures capable of denaturizing hydrogel material, the heating time is sufficiently short that the heating has no detrimental effect on the stability of biocomponents [45].

2.2.5. Piezoelectric inkjet bioprinting

Another drop-on-demand approach, piezoelectric inkjet printing implements a piezoelectric actuator to form droplets (Fig. 2E). A piezoelectric crystal within the print head is stimulated by an applied voltage, which induces a rapid, reversible deformation [1]. This deformation causes a sudden change in volume of the bioink chamber, resulting in the propagation of acoustic waves [46,47]. These acoustic waves then supply the pulse of pressure needed to exceed the surface tension at the nozzle orifice, disrupting the flow of ink through the print head, thereby producing droplets. To improve the efficiency and reliability of the printing process, studies have focused on optimizing the bioink constituents, piezoelectric element actuation modes, and voltage pulse characteristics [48–51].

2.2.6. Electrostatic bioprinting

The third type of drop-on-demand inkjet printer is electrostatic printing. Functioning in a similar manner to piezoelectric inkjet bioprinting, electrostatic bioprinting generates droplets by momentarily increasing the volume of the fluid chamber (Fig. 2F) [52]. Instead of a piezoelectric crystal, this technique implements a pressure plate. By applying a voltage pulse between the pressure plate and an electrode, the pressure plate deflects, thereby ejecting droplets from the nozzle [53].

2.2.7. Electrohydrodynamic jet bioprinting

Electrohydrodynamic jet bioprinting generates droplets on a drop-by-drop basis, similar to the three drop-on-demand inkjet printing approaches. The difference arises in the formation of the droplet: drop-on-demand inkjet bioprinters apply pressure to the bioink, whereas electrohydrodynamic bioprinters use an electric field to pull bioink through an orifice [54]. Electrohydrodynamic jetting operates by feeding the bioink solution through a metallic nozzle with just enough back pressure to form a spherical meniscus at the tip of the nozzle (Fig. 2G) [54–57]. A high voltage is then applied between the nozzle and the receiving substrate which generates an electric field between them [55,58]. The electric field produces an accumulation of ions in the bioink, and the electrostatic repulsions between the ions deform the meniscus at the nozzle's tip into a conical shape. As the electrostatic stresses overcome the surface tensions at the orifice, bioink is ejected. The form of the ejected bioink, known as the jetting mode, is determined

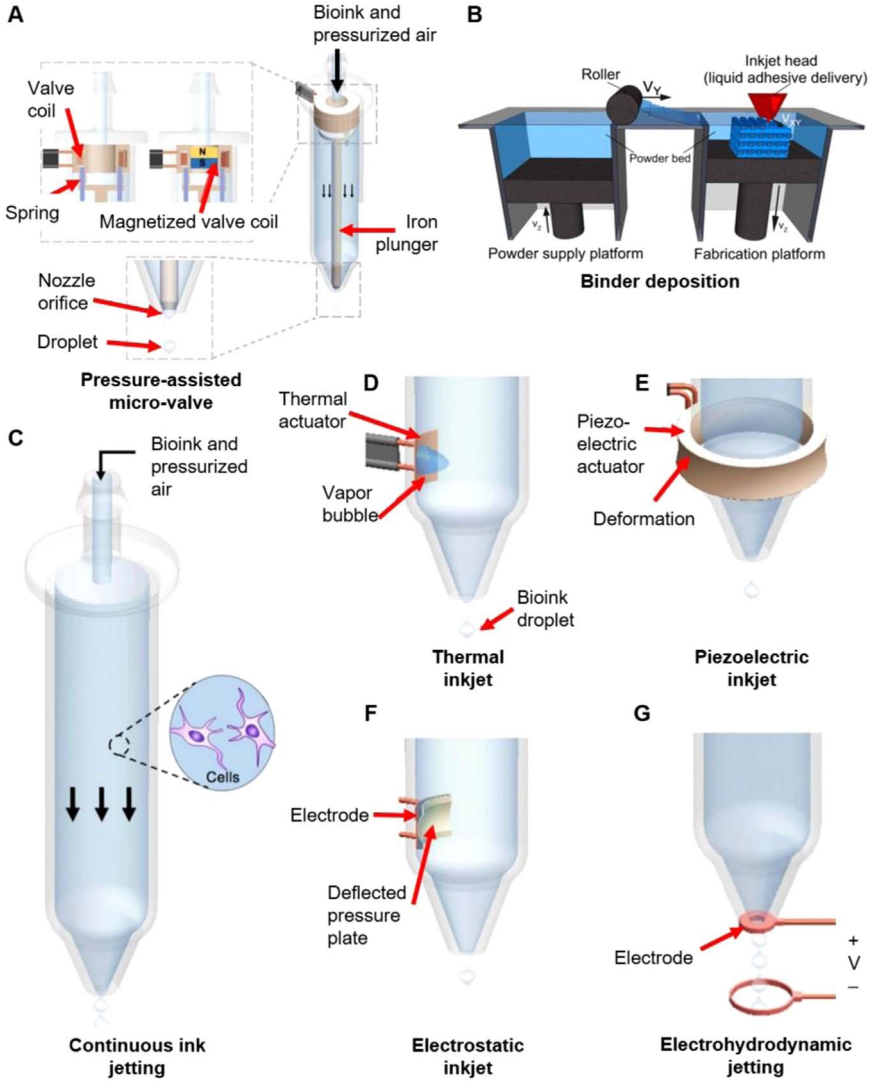

Fig. 2. Droplet-based printing techniques. (A) Pressure-assisted micro-valve bioprinting [16]. A micro-valve bioprinter consists of a pressurized reservoir of liquid bioink and a nozzle with an electromechanical micro-valve. When a magnetic field is produced, the plunger moves upwards, unblocking the orifice in the nozzle. Reproduced, with permission, from [16]. (B) Binder deposition [18]. Inkjet printing techniques can be applied to binder deposition, in which a binding solution is deposited into a bed of loose photosensitive powder or un-crosslinked photosensitive liquid. Reproduced, with permission, from [18]. (C) Continuous ink jetting [16]. Bioink is continuously jetted from the nozzle in the form of a stream of discrete droplets formed by the Rayleigh-Plateau instability. (D–G) Drop-on-demand printing techniques [16]. Drops are formed on an individual, controlled basis. (D) Thermal inkjet printing. A thermal actuator momentarily vaporizes the bioink producing a vapor bubble. The pressure from the expansion and collapse of the bubble forces a droplet out of the nozzle. (E) Piezoelectric inkjet printing. In response to an applied voltage, a piezoelectric crystal induces a rapid, reversible deformation in the bioink chamber, and thereby a volumetric change which produces a droplet. (F) Electrostatic inkjet printing. An applied voltage pulse between the pressure plate and an electrode cause the plate to deflect. The plate's deflection causes a volume change which forces out a droplet. (G) Electrohydrodynamic jetting. A high voltage is applied between the nozzle and the receiving substrate to generate an electric field. The electric field causes an accumulation of ions in the bioink, and the electrostatic repulsions between the ions deform the meniscus at the nozzle's tip into a conical shape. As the electrostatic stresses overcome the surface tensions at the orifice, bioink is ejected. Reproduced, with permission, from [16].

by the voltage applied: low voltage resulting in dripping, intermediate voltage produces distinct droplets, and high voltage produces a continuous stream [54,59]. The strength of the electric field, in addition to the flow rate of the bioink and the bioink properties, affects the long-term post-bioprinting cell viability [60]. Also related to cell viability, by relying on the electric field to generate droplets, this technique alleviates the need for high pressure which can be damaging to cells contained within the bioink. Furthermore, electrohydrodynamic jetting is particularly well-suited for applications involving very small orifice diameters and highly concentrated bioinks, referring to both hydrogel weight per volume and cell concentration [61].

2.2.8. Additional techniques

Inkjet printing is implemented for binder deposition, a 3D printing technology which functions, most often, by depositing a liquid binder solution into a bed of thermal-sensitive powder [62–64]. The powder is spread over the build surface by a roller and pressed to form the appropriate layer thickness. The binder solution is spotted onto the powder by one of the aforementioned inkjet printing techniques (Fig. 2B). Upon contact with the powder, the binder solution causes adjacent powder particles to bind into a solid form. For each layer, the bed is lowered and a new layer of powder is rolled. This technique is compatible with several materials including ceramics, metals, polymer, and even hydrogels [65–68]. Binder deposition can also be adapted by replacing the powder bed with a vat of liquid material [69]. The binder solution then takes the form of a liquid crosslinking initiator while the vat of liquid contains un-crosslinked hydrogel.

2.3. Laser-based printing techniques

Laser-based techniques for 3D bioprinting can be divided into two types: those in which the laser is used to collect printed material on a

receiving substrate, and those in which the laser builds the 3D constructs from a bulk medium. The former can further be classified into laser-guided direct writing and laser-induced forward transfer [70]. For both of these techniques, the laser is used to form or deposit a droplet, similar to the droplet-based techniques from above. As for techniques which build from a vat of bulk material, the laser-based bioprinter builds 3D structures by curing layers of photocurable material [18,71]. These techniques include stereolithography and digital light projection. Generally speaking, such laser-based printing techniques are very high resolution and relatively fast. Additional laser-based 3D printing techniques that have not yet been applied for bioprinting, two-photon polymerization and solid ground curing, are also described.

2.3.1. Laser-guided direct writing

Laser-guided direct writing is a laser-driven, droplet-based bioprinting technique [72,73]. A weakly focused laser beam is directed towards a cell suspension, optically traps cells, and then guides them onto a receiving substrate (Fig. 3A) [74–77]. Effectively, this technique leverages the difference in the refractive indices of cells and surrounding media to trap and guide them onto the receiving substrate below the cell suspension. Since this technique is dependent on refractive indices, and consequently the optical trapping forces, laser-guided writing is limited to very few compatible materials and biologics [76].

2.3.2. Laser-induced forward transfer

Similar to the laser-guided writing approach, laser-induced forward transfer uses a laser to form droplets [77]. Laser-induced forward transfer bioprinters consist of three main components: a pulsed laser source, a laser-absorbing interlayer made of a quartz ribbon, and a receiving substrate (Fig. 3B) [70,78]. Focused laser pulses from above locally heat the bioink through the interlayer. The localized heating causes a vapor bubble in the bioink to rapidly expand and collapse, sending a pressure wave through the medium. This pressure wave propagates through the bioink, forcing droplets to be ejected from the interlayer ribbon down to the receiving substrate [79–81]. The size and frequency of droplets can be manipulated by controlling parameters such as the bioink viscosity and laser intensity.

2.3.3. Stereolithography

Using a computer-controlled ultraviolet (UV) laser, a stereolithography bioprinter functions by focusing the laser within a vat of hydrogel or resin which is made to be photosensitive by the addition of a photo-initiator (Fig. 3C) [82]. Upon exposure to the UV laser, the liquid solidifies; specifically, the energy provided by the laser results in the formation of covalent bonds between adjacent polymer chains. For each layer, the laser scans across a 2D pattern [18]. By submerging the stage in the vat of liquid and moving it up/down a distance equal to the layer height, the material is built in layers to form the final 3D construct [18,83]. The resolution of a stereolithography bioprinter is dependent on various factors, including the power of the laser, scanning speed, exposure time, laser-spot size, and the wavelength of light used [83]. Given the precision of this technique and the ability to fine tune the aforementioned parameters, stereolithography offers very high printing resolution. Furthermore, recent advances have been made in micro-stereolithography, using both scanning, described above, and masking approaches [84,85]. Masking involves the use of a physical mask to strategically block out light while letting a specific light pattern to pass through to the vat of material; the material exposed to the non-blocked light cures to form a layer.

2.3.4. Digital light projection

Digital light projection follows the masking approach of stereolithography, whereby an entire layer is exposed at once. The same vat of photosensitive material is used here as in stereolithography, providing an automatic supply of fresh material during the printing process as the stage rises [18]. Rather using a physical mask to block and filter the light to produce the exposed area, digital light projection uses a digital mirror device or liquid crystal displays to directly provide a light pattern (Fig. 3D) [18]. Several mirrors or LCD pixels combine to form a dynamic pattern generator which switches on/off between each layer and reconfigures to pattern different layers. Owing to this precise manner of patterning, digital light projection allows for very high resolution, reportedly between 25 and 150 μm, which can be further refined by lens systems to focus the light source [18,83].

2.3.5. Additional techniques

Two-photon polymerization is a new, advanced stereolithographic approach to fabricating nano-scale structures. Instead of a typical UV laser, two-photon polymerization relies on femtosecond pulses of an infrared laser which is focused into a volume of photocurable liquid material (Fig. 3E) [18,83,86]. The infrared laser light used benefits from nonlinear behavior and the existence of a polymerization threshold, which allows for direct fabrication of 3D structures within the vat of liquid with extremely high resolution down to a focal spot size of 200 nm [18,83]. At the focal spot of the laser pulses, photolytic polymerization of the material occurs without the need for any sort of masking. Specifically, two high-intensity laser beams are focused at the same spot, providing two photons to the liquid in that spot; the photons provide the excitation energy required for the photo-initiator contained within the liquid to produce free radicals. The free radicals break unstable bonds of the monomers in the liquid, thereby initiating the polymerization process as the monomers form into chains. Unsurprisingly, the high resolution and precision of this method also makes it considerably more complicated: insufficient free radical density and the minuscule focusing area make this method difficult to implement [87,88]. Nonetheless, two-photon polymerization proves to be a promising 3D printing technique that can be used for bioprinting. Since infrared light is harmless to living cells, cell-laden structures can be directly printed [89]. Additionally, since this method is not a layer-by-layer approach and operates without masks, 3D structures containing pores can be fabricated, which is impossible using other bioprinting techniques; such pores enable the precise control of cell position, movement, and organization within bioprinted tissues [88,89].

Another stereolithography-based technique is solid ground curing. Using the masking approach, solid ground curing implements a high-powered UV lamp filtered by a patterned mask placed between the lamp and photosensitive material [83,90,91]. The mask is machine-fabricated on glass, requiring separate masks for each individual, distinct layer. What makes solid ground curing different from traditional stereolithography is an intermediate process performed between each layer [83,90]. Each layer begins with a spray application of fresh photocurable material, as opposed to the submerging that occurs in the previously mentioned techniques. After UV irradiation, uncured material is removed by vacuum while the remaining cured material is filled with wax for support, allowing for overhanging material to be printed in subsequent layers. After printing, the wax is melted to reveal the 3D structure. This laser-based 3D printing technique has not been applied for bioprinting but may be adapted to help fabricate more complex structures in tissue engineering.

3. The importance of computational modeling for bioprinting

There is strong experimental evidence that many geometrical features and controllable material properties can have significant effects on cell viability and proper formation of the desired tissue structure. Given the vast number of possible combinations of geometrical metrics and material properties, in addition to the abundance of bioprinting methods available, it only makes sense to develop and utilize computational models to develop a better understanding of the

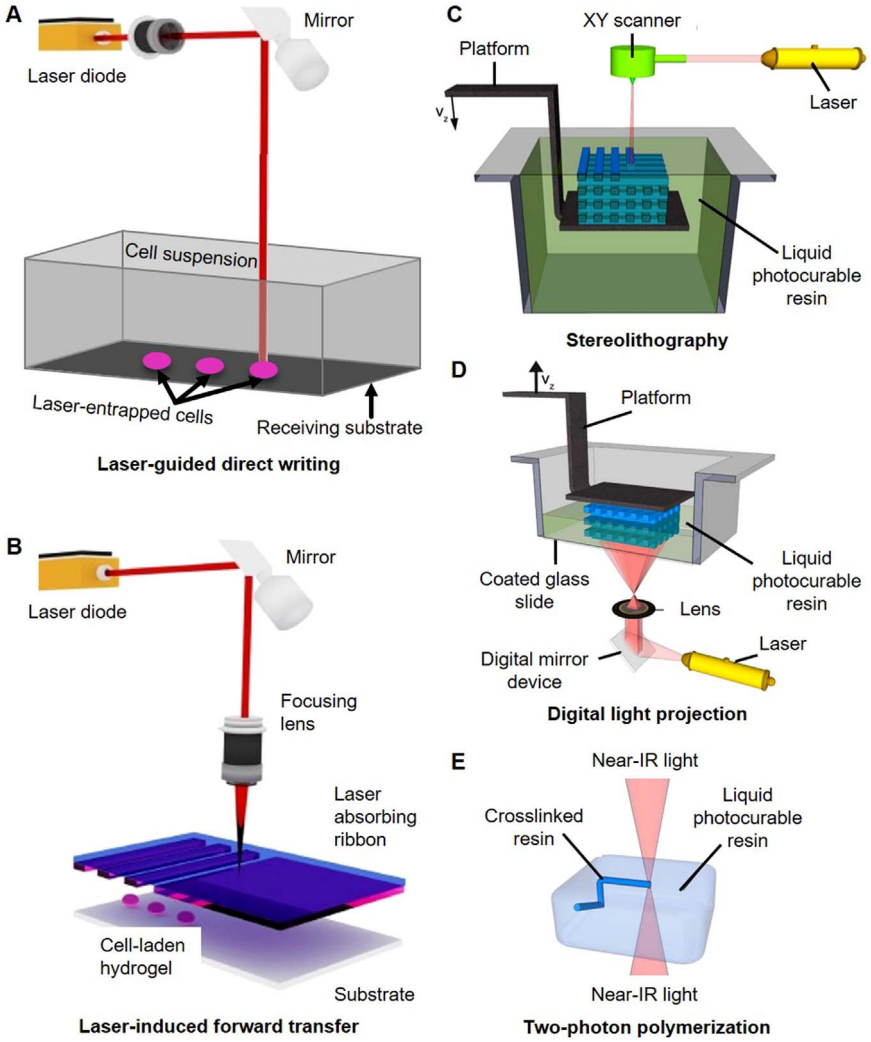

Fig. 3. Laser-based printing techniques. (A) Laser-guided direct writing [6]. A laser directed towards a cell suspension guides the cells from the suspension to a receiving substrate by optical entrapment. (B) Laser-induced forward transfer [6]. A laser is focused on a laser absorbing ribbon which carries cell-laden hydrogel beneath it. The energy from the laser causes droplets to form off of the ribbon and onto a receiving substrate. Reproduced, with permission, from [6]. (C) Stereolithography [18]. The printed structure is formed from a vat of bulk photocurable material by scanning a laser at the surface of the liquid following a computer-generated 2D pattern. As each layer is cured, the platform is raised/lowered to replenish the liquid material at the surface. (D) Digital light projection [18]. Using the same vat of liquid material as stereolithography, digital light projection uses a digital mirror device or liquid crystal displays to directly provide a light pattern. Rather than a scanning laser as in stereolithography, digital light projection exposes an entire layer at once by using several mirrors or LCD pixels to form a dynamic pattern generator. (E) Two-photon polymerization [18]. Two high-intensity infrared lasers are focused at the same spot within a volume of liquid. Laser pulses provide two photons to the liquid; the photons provide the excitation energy required for the photo-initiator contained within the liquid to produce free radicals which break the unstable bonds of the monomers in the liquid, thereby initiating the polymerization process as the monomers form into chains. Reproduced, with permission, from [18].

bioprinting process, rather than relying solely on experimental research. For instance, the long-term viability and culture of cells within encapsulating droplets has been shown to be highly dependent on the relative location of the cell within the droplet. Kamperman et al. showed that off-center encapsulated cells that touched the outer edge of the droplet often protruded and subsequently escaped from the droplet within a few days after droplet formation (Fig. 4A) [92]. The off-centered location of cells can adversely affect the interaction of the hydrogel droplet with biochemical and biomechanical stimuli that play important roles in cell culturing. If cells are positioned at the interface of the droplet within the first milliseconds of droplet formation, the cells are then predisposed to being off-center. Using a typical crosslinking scheme, the hydrogel is immediately gelled after deposition, locking the cell into this off-center position. Conversely, delayed enzymatic crosslinking was shown to outperform more common physical and photo-crosslinking hydrogels systems by allowing for the cell to re-center before gelling [92]. Delayed enzymatic crosslinking results in higher levels of cell survival, metabolic activity, and multilineage differentiation over a prolonged period of time (Fig. 4B,C). Computational methods should be introduced to model the effect of droplet generation and crosslinking mechanisms in order to predict cell viability.

Computational modeling can be applied to several other applications pertaining to cell survival and geometrical integrity. One such application is predicting the effect of dispensing pressure and nozzle diameter on the viability and functional behavior of cells in solid freeform bioprinting. Experimental results have revealed mechanical damage to cell membrane integrity caused by the bioprinting process, marked by a quantifiable loss in cell viability [93]. For creating full-scale tissues and organs, blood-vessel-like channels would need to be bioprinted to provide channels for nutrient transport and waste removal. Tubular, cell encapsulating channels have been demonstrated by Yu et al. The direct fabrication of the cell-laden tubular channels was facilitated by a custom coaxial nozzle assembly, which showed a direct correlation between cell survival and various printing parameters, including dispensing pressure, coaxial nozzle geometry, and biomaterial concentration [94]. Again, computational modeling can be implemented to purposefully design the coaxial nozzle to yield optimum cell

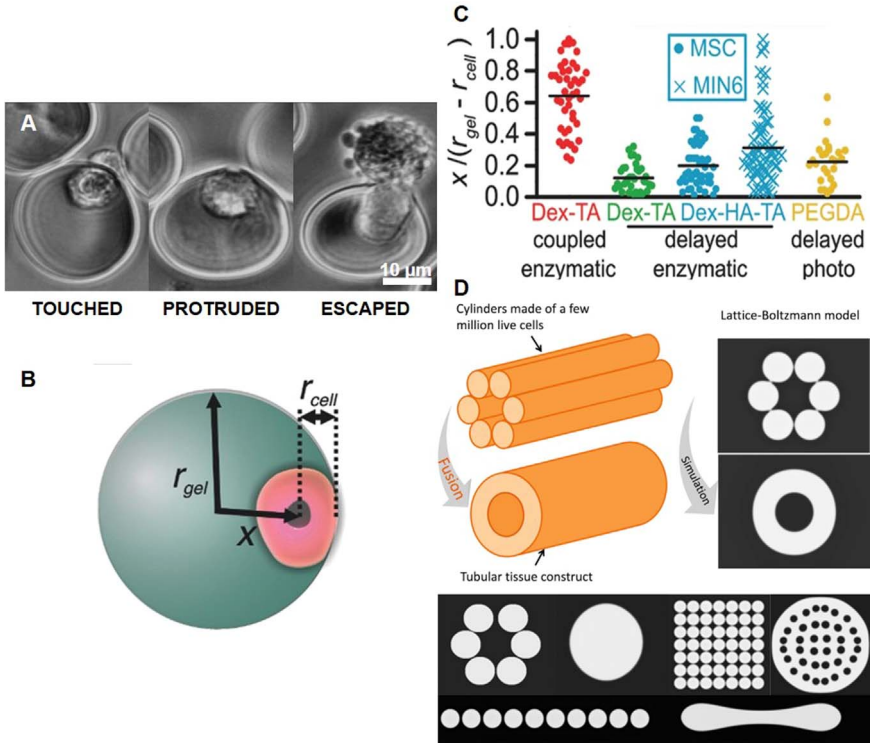

Fig. 4. Examples of the usefulness of computational modeling for improving cell viability and geometrical integrity. (A–C) Analysis and control of cell position within encapsulating droplet [92]. (A) Off-center encapsulated cells that are touching the boundary of the droplet, protruding from the droplet, or have escaped from the droplet entirely, which adversely affects the viability of the cells. (B) The position of the cell within the encapsulating hydrogel droplet was quantified by $\frac{x}{(r_{gel} - r_{cell})}$ with x, r_{gel}, and r_{cell} as the distance from the cell's center to the hydrogel's wall, and diameters of the hydrogel and cell, respectively. (C) Cell position analyses of various combinations of distinct hydrogel materials (Dextran-tyramine, Dextran-hyaluronic acid-tyramine, and Poly(ethylene glycol) diacrylate), cell types (MIN6, MSC), and crosslinking methods (enzyme-based, delayed enzyme-based, and delayed photo-crosslinking). Delayed crosslinking exhibited increased cell-centering, as compared to the conventional microfluidic encapsulation approach where emulsification and gelation are coupled. Reproduced, with permission, from [92]. (D) The fusion of multicellular cylinders, shown as snapshots of a two-dimensional Lattice Boltzmann simulation that models the evolution of the transversal cross-sectional [97]. Images show the morphogenesis of the following configurations: a hexagonal arrangement which fuses into a tubular cylinder, a defective hexagonal arrangement with two misplaced cylinders which results in a solid cylinder, a contiguous square lattice which fuses into a tissue-like construct, and a planar arrangement which fuses into a sheet-like structure. Reproduced, with permission, from [97].

viability results, as opposed to a lengthier, and likely costlier, iterative approach involving the design, fabrication, and experimental testing of different nozzles.

Justifiably, a significant amount of work has been conducted to apply computational modeling to bioprinting for these purposes. The effect of needle geometry and air pressure has been studied experimentally and correspondingly simulated by models to specify the influence of process parameters on the flow rate of cell-laden printing material and the cell viability within the printed structures [95]. The models are useful for optimizing process parameters with the goal of preserving cell viability and achieving the desired cell distribution. Computational modeling has also been demonstrated to create well-designed tissue engineering constructs using a specific spatial pattern of cells in a matrix to improve tissue and bone regeneration [96]. Specifically, a cell-gradient pattern of cell-laden hydrogels consisting of varying cell densities yielded a higher cell viability post-printing, as compared to uniform constructs. In addition to using computational modeling to simulate the bioprinting process itself, computational methods can be used to study the mechanisms involved in the fusion of multicellular constructs. For instance, using the Lattice Boltzmann method, post-printing rearrangement of cells was simulated to predict the geometry and stability of printed structures [97]. Several shapes were tested, including a hexagonal formation of cylinders which fuses into a cylindrical tube, a defective hexagon, a square lattice which fuses into a tissue-like structure, and a series of cylinders which fuses into a planar construct (Fig. 4D). Such simulations allow for new working hypotheses to be tested in a faster and lower-cost manner than in the laboratory.

From the works described – notably just a few reports from a wide realm of bioprinting, computational modeling, and cell viability studies – it is clear that computational modeling can be an extremely powerful and useful tool in optimizing the cell viability and geometrical integrity of bioprinted constructs. In the following sections, computational models are discussed for application to bioprinting and post-printing fusion of printed constructs. For the process of bioprinting itself, computational methods are discussed for droplet-based bioprinting, extrusion-based bioprinting, and the ability to set experimental parameters with informed decisions via modeling.

4. Computational models applied to droplet-based bioprinting

4.1. Compound droplet impact model: Newtonian-model

Cells may be modeled as Newtonian droplets whose viscosity is significantly higher than that of the ambient fluid. This is accomplished by simplifying the complicated internal structures of cells into an apparent viscosity. Assuming a Newtonian model, the fluid motion of the impact and spreading of a compact droplet is governed by the incompressible Navier-Stokes equations. Although an oversimplification, the cell is modeled as a highly viscous inner droplet surrounded by encapsulating liquid and surrounding air, all of which are assumed to be Newtonian fluids with different material and interfacial properties [15]. A finite-difference front-tracking method from Unverdi and Tryggvason [98] and Tryggvason et al. [99] was implemented by Tasoglu et al. [15,100]. By this computational method, a separate Lagrangian grid is used to track the interfaces between the inner and outer droplets and between the outer droplet and the surrounding

fluid. Each Lagrangian grid consists of linked marker points that move with the local flow velocity, which itself is interpolated from a stationary Eulerian grid. The surface tension is then determined from the Lagrangian grid, which is then distributed onto Eulerian grid points near the interface using Peskin's [101] cosine distribution function; the surface tension is also added to the momentum equations as body forces, as described by Tryggvason et al. [99]. At each time step, the fluid properties inside and outside the droplet are computed by an indicator function, which requires the solution of a separable Poisson equation, yielding a smooth transition across the interface. This is accomplished by distributing unit magnitude jumps in a conservative manner on the Eulerian grid points near the interfaces using Peskin's [101] cosine distribution function followed by integrating them to compute the indicator function everywhere. With each time step, the Lagrangian grid is restructured by deleting the front elements, portions of the Langragian grid between two marker points, that are smaller than a specified lower limit and splitting the front elements that are larger than a specified upper limit. This maintains the front element size to be nearly uniform and comparable to the Eulerian grid size.

Using the front-tracking finite-difference method described, the impact of a compound droplet on a flat surface was computational modeled for a variety of parameters [15]. The relaxation of a compound droplet from a spherical initial condition to its final equilibrium shape was studied for various values of the Eötvös number, which is representative of the ratio of gravitational and surface tension forces. With the density of the inner and encapsulating droplets equal, as well as the respectively viscosities being set equal, the test case becomes equivalent to a simple droplet when the ratio of surface tension coefficients is large [100]. The static shape of the droplet generally is dependent on the equilibrium contact angle, the Eötvös number, and the ratio of surface tension coefficients. When Eötvös number is very small, the equilibrium shape of the droplet is then dependent on the surface tension force and the encapsulating droplet forms a spherical cap. Conversely, when the Eötvös number is large, the shape of the compound droplet is dominated by gravitational and surface tension forces. These findings are in agreement with the normalized static droplet height as a function of Eötvös number, presented in Fig. 5A [15]. The computed normalized droplet height agrees well with the asymptotic solutions when the Eötvös number is very small or large, and the difference between the computational and asymptotic solutions decrease monotonically as the Eötvös number increases. However, the solution deviates from the asymptotic solution for large Eötvös numbers as the surface tension coefficient ratio increases. A base case of dimensionless parameters $We = 0.5$, $Re = 30$, $\frac{d_o}{d_i} = 2.85$, $\frac{\sigma_0}{\sigma_i} = 2541$, and $\frac{\mu_c}{\mu_d} = 10$ was selected based on experimental data and consideration for numerical stability and convergence. For this base case, the shape evolution of the impact and spreading of a compound droplet can be seen in Fig. 5B (initial shape) and 6C (shape after some passing of time) [15]. From this base case, the effects of each non-dimensional number were also studied by systematically varying its value while keeping all other parameters equal to the base case. The deformation and rate of deformation of cell as a function of dimensionless time were studied for varying Reynolds numbers, $Re = 15$, 20, 30, 40, and 45 (Fig. 6A) [15]. The maximum deformation and rate of deformation was shown to increase as Reynolds number increases. The deformation and rate of deformation of the cell was also plotted for varying Weber numbers, $We = 0.25$, 0.5, 1.0, 2.0, 5.0, and 10.0 (Fig. 6B, C) [15]. The maximum spread initially decreases as Weber number increases, then starts to increase with increasing weber number. Additionally, it can be seen that the encapsulating droplet reaches equilibrium faster as Weber number decreases. Deformation first decrease with Weber number until $We = 2$, then increases with increasing Weber number. However, the rate of deformation consistently decreases as the Weber number increases.

4.2. Viscoelastic features

In addition to modeling droplet-based bioprinting by Newtonian droplets, viscoelastic features should also be considered. The bioinks used in bioprinting surround cells in encapsulating droplets, as previously described. The bioink effectively provides a barrier of protection for the cells against stresses during the bioprinting process. In particular, bioinks consist of polymers of long-chain molecules, and thereby exhibit viscoelastic behavior [102]. Additionally, the cells themselves contain proteins which are composed of long-chain molecules, as well. Since both the cell and the cell-encapsulating droplet possess long-chain molecules capable of viscoelastic behavior, it is easy to justify the implementation of a viscoelastic model for droplet-based bioprinting. Consequently, it is fundamentally important to understand the effects of viscoelasticity on the bioprinting process.

Numerous studies of droplets and cells have reported numerical simulations which factor in viscoelastic effects. For instance, Khismatullin and Truskey implemented a three-dimensional numerical simulation which included the effects of cell deformability and viscoelasticity to study receptor-mediate leukocyte adhesion to surfaces [103]. Luo et al. modeled leukocytes as compound viscoelastic capsules with a nucleus and investigated the effects of cell length, inclination angle, and drag and lift forces on the flow dynamics of a nucleated cell tethered under shear flow [104]. Chung et al. studied the effect of viscoelasticity on drop dynamics in microchannel flow [105]. Specifically, they investigated the drop dynamics for various viscosity ratios between the droplet and medium, capillary numbers, droplet sizes, and values of fluid elasticity. Their result showed that viscoelasticity plays an important role in drop dynamics with increasing viscosity ratios for a Newtonian droplet in a viscoelastic medium. Chung et al. had also previously studied the effect of viscoelasticity on drop deformation in simple shear through a planar contraction/expansion microchannel [106]. In this case, in addition to a Newtonian drop in a viscoelastic medium, a Newtonian drop suspended in a viscoelastic medium was also considered, demonstrating the significant role that viscoelasticity plays on drop dynamics and drop shape, which may prove useful in the modeling of bioprinting. Despite the varied focused of these previous studies, they demonstrate the capability of modeling droplets with viscoelastic features.

Using these works as a foundation, future work can be performed to create computational models to study the effects of viscoelasticity in the bioprinting process [107]. For instance, Izbassarov et al. implemented a front-tracking method to computationally study the effects of viscoelasticity of bio-inks on cell viability during the deposition of cell-laden droplets on a substrate. The cell and encapsulating droplet were modeled as viscoelastic liquids, while the ambient fluid was Newtonian. They showed that the Weissenberg number, which compares the elastic forces to the viscous forces, and the polymeric viscosity ratio have a significant influence over cell viability and can be useful parameters in controlling and improving droplet-based bioprinting systems [107]. Promising results, particularly for application to bioprinting, demonstrated that viscoelasticity of the encapsulating droplet actually enhances cell viability.

5. Computational models applied to extrusion-based bioprinting

5.1. Cell viability

Computational models are not limited to droplet-based bioprinting; Nair et al. has demonstrated a quantitative model for cell viability prediction from process parameters and induced shear forces which was used to model extrusion-based bioprinting [108]. More precisely, the model considered the effects of dispensing pressure and nozzle size on cell viability which was validated experimentally. During the extrusion process, similar to the droplet-based printing modeled by

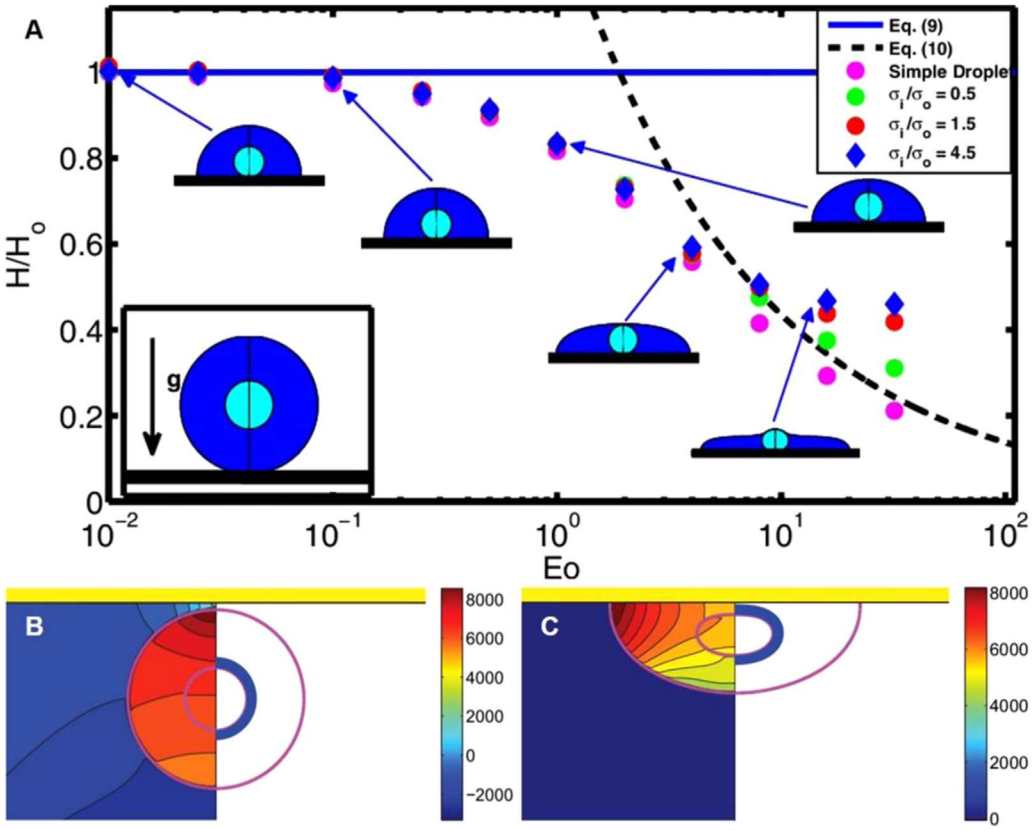

Fig. 5. Compound droplet impacting on a flat surface [15]. (A) Normalized static droplet height vs Eötvös number for the range $Eo = 0.01$ to $Eo = 64$. Solid and dashed lines denote the analytical solutions for the limiting cases of $Eo \ll 1$ and $Eo \gg 1$, respectively. The inset image depicts the initial conditions for the droplet relaxation test. The computed normalized droplet height agrees well with the asymptotic solutions; the difference between the computational and asymptotic solutions decrease monotonically as the Eötvös number increases. (B, C) Compound droplet impacting on a flat surface, where the left-half depicts the pressure contours and right-half depicts the pressure distribution on the surface of the cell, for the following conditions: $We = 0.5$, $Re = 30$, $\frac{d_o}{d_i} = 2.85$, $\frac{\sigma_0}{\sigma_i} = 2541$, and $\frac{\mu_c}{\mu_d} = 10$. (B) Snapshot at $t^* = 0.000269$. (C) Snapshot at $t^* = 0.5135$. Reproduced, with permission, from [15].

Blaeser et al., shear stresses imposed on the cell-laden hydrogel can have negative effects on cell viability. A factor influencing the amount of shear stress at the tip is the nozzle size, while the applied dispensing pressure induces compression or tensile forces on the printing material [108]. With this knowledge, the goal was to develop a mathematical model to predict the state of the cell as a function of the shear stresses induced by the system to assist in optimizing the printing process, as well as in studying the effects of process-induced mechanical perturbations on cell viability. Experimentally, Nair et al. assessed a proprietary pressure-driven bioprinter capable of solid freeform fabrication. The bioprinter operated a room temperature and was controlled by manipulating the dispensing pressure. Experiments were conducted by printing at various air pressures, from 5–40 psi using nozzle diameters within the range of 150 – 400 microns. Results indicated a decrease in the percentage of live cells with increasing dispensing pressure and decreasing nozzle diameter [108].

The experimental results were used to derive a quantitative model relating cell viability to process parameters, namely the dispensing pressure and the nozzle diameter. The first model expressed the expected value for the percentage of live cells, injured cells, and dead cells as a function of the two independent variables, with constants derived by correlating to the experimental data [108]. An analytical model was also developed to predict the maximum shear stress within the nozzle of the bioprinter based on the assumption that alginate, the chosen hydrogel for the experiments, is a non-Newtonian fluid [109]. The power-law function was used to relate shear stress with the apparent shear rate, where the wall shear rate was expressed as proportional to the deposition speed and inversely proportional to the nozzle radius. The deposition speed was related to the deposition flow rate by the cross-sectional area of the nozzle. The relationship between the flow rate and the process and material parameters was derived by generalizing Poiseuille's equation for an incompressible, non-Newtonian fluid flow through a uniform circular cross-section. As an extension of this model, the maximum shear stress was used to predict cell viability by combining the quantitative model for cell viability and process parameters with the shear stress model, resulting in a predictive curve to determine the percentage of live cells for a given set of process parameters and a given shear stress (Fig. 7) [108]. Resultingly, the combination of these two models provides an effective way to predict cell viability as a function of the maximum shear forced, which itself is caused by various process parameters.

5.2. Shape fidelity

The shape fidelity of extruded biomaterial has also been studied and modeled. Bioprinted filaments should exhibit shear thinning behavior, meaning that its viscosity decreases with increasing shear rate [110]. The filament should also have sufficient yield stress and quick recovery kinetics, such that it behaves as a non-viscous liquid during extrusion. Important for bioprinting geometrically and structurally accurate structures, the filament must form a stable gel quickly after deposition [111]. However, the rheological properties ideal for the shape fidelity of bioprinted forms requires a compromise with biocompatibility. Namely, the ability of encapsulated cells to proliferate, differentiation, and actively function may be adversely affected as the filament becomes more structurally rigid [111]. Due to this balancing act in implementing different bioinks, the printability of the material should be carefully evaluated in order to assess the physical deformation of the deposited filament, predict the shape fidelity of the printed structure, and precisely control deposition during the bioprinting process.

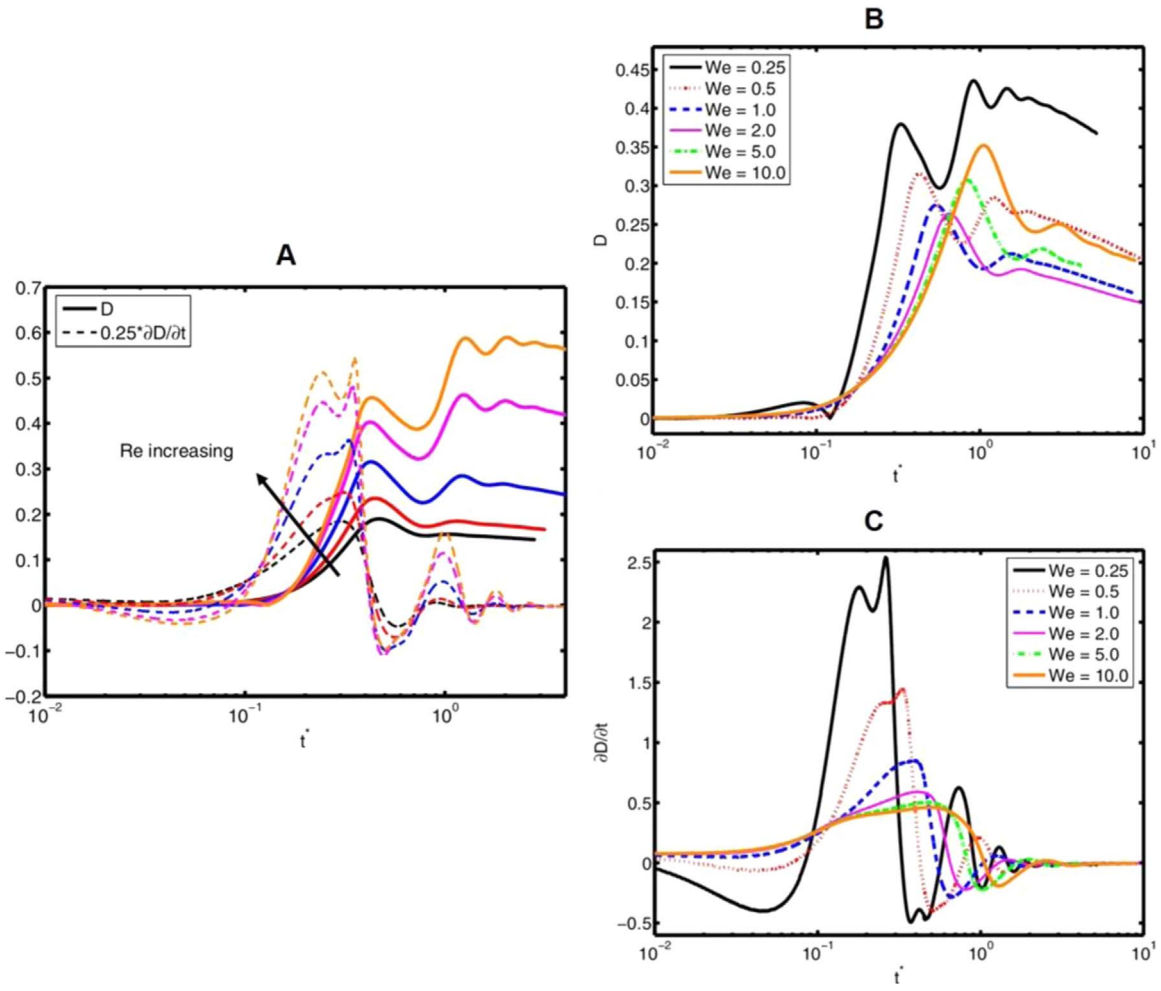

Fig. 6. Deformation and rate of deformation for various Reynolds and Weber numbers [15]. (A) Deformation and rate of deformation vs. non-dimensional time for $Re = 15, 20, 30, 40,$ and 45 for the following conditions: $We = 0.5$, $\frac{d_o}{d_i} = 2.85$, $\frac{\sigma_0}{\sigma_i} = 2541$, and $\frac{\mu_c}{\mu_d} = 10$. Peak cell deformation and rate of deformation increase as Reynolds number increases. (B) Deformation and (C) rate of deformation vs. non-dimensional time for $We = 0.25, 0.5, 1.0, 2.0, 5.0,$ and 10.0 for the following conditions: $Re = 30$, $\frac{d_o}{d_i} = 2.85$, $\frac{\sigma_0}{\sigma_i} = 2541$, and $\frac{\mu_c}{\mu_d} = 10$. The encapsulating droplet reaches equilibrium conditions faster as Weber number decreases. Deformation first decreases with Weber number until $We = 2$, then increases with increasing Weber number. The maximum rate of deformation consistently decreases as Weber number increases. Reproduced, with permission, from [15].

During any extrusion-based 3D-printing process, inclusive of bioprinting, deformation may occur in the form of collapsed overhanging filaments and the fusion of adjacent filaments. When such deformations occur, the ability to build successive layers with desired resolution and pore structure is compromised [112]. While it is rather simple to qualitatively assess shape fidelity via visual inspection of printed constructs, Ribeiro et al. took this a step further by introducing a quantitative method for evaluating the shape fidelity of extruded bioinks based on a filament collapse test by Therriault et al., which measured the mid-span deflection of a suspended filament, and a test for the filament fusion of parallel printed strands [113]. By this method, the ability of extruded bioink to support itself was characterized by direct video imaging. Bioinks of poloxamer 407 and poly(-ethylene glycol) blends were tested to provide a range of hydrogels with varying yield stresses.

In Ribeiro et al.'s work, the theoretical model for predicting the shape fidelity of extruded bioink filaments assumed that after 20 s of bioprinting, the deformation becomes negligible and the forces acting on the bioprinted filament reaches equilibrium [112]. Specifically, the force of gravity and the force resulting from the filament's resistance to yield must sum to zero (Newton's Second Law of Motion for motionless objects), where the vertical component of the resistance to yield is a function of the deflection angle, measured between the filament and the horizontal plane. By considering an infinitesimal volume element of the filament, the angle of deflection can be related to the stresses acting on the volume. Results of the filament collapse test showed that filament sagging increased as the gap length between underlying filament strands increased, as evidenced by an increase in the deflection angle. Additionally, an increase in yield stress resulted in a decrease in sagging. The experimental results were compared to numerical predictions; although both experimental and theoretical results displayed a linear relationship between gap length and deflection angle, discrepancies were also revealed [112]. Furthermore, results from the filament fusion test showed a nonlinear inverse relation between the fused segment length, or the length of printed filament that self-fuses, and the filament distance, or the distance between parallel filaments. In both tests performed, an increase in the gel concentration resulted in improved shape fidelity. These results demonstrate parameters relevant to shape fidelity of extruded filaments which may be used within computational models. In Therriault et al.'s work, the experimentally observed behavior of the filament collapse test was also compared to numerical predictions based on a simple theoretical model relating filament collapse with the yield stress of the bioink [112,113]. Specifically, the printed filament was modeled using beam mechanics. An expression from the quasi-static form of Euler-Bernoulli viscoelastic beam theory was used to create a model for the time-dependent mid-span deflection of a filament, which showed good agreement with normalized experimental behavior [113]. These

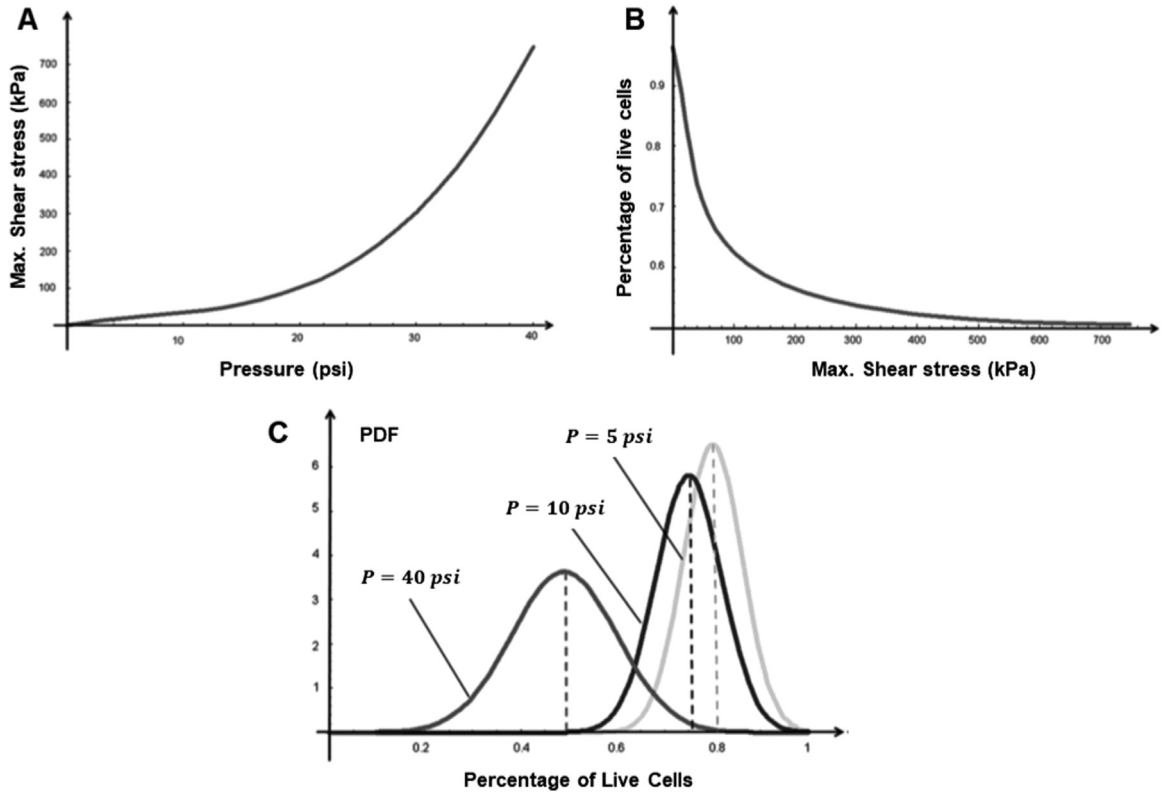

Fig. 7. Mathematical modeling results for the effect of shear stress on cell viability for extrusion-based bioprinting [108]. (A) Maximum shear stress versus dispensing pressure for nozzle diameter of 250 microns. The model predicts a non-linear increase in maximum shear force with increasing pressure. (B) Percentage of cell viability versus maximum shear stress. (C) Probability density function (PDF) distributions for a nozzle diameter of 150 microns at various pressures. Reproduced, with permission, from [108].

studies of the shape fidelity of extrusion-based bioprinting are a necessary component in computationally predicting the results of various printing and geometrical parameters, as the ability to predict the shape fidelity of printed structures is crucial for improving printing resolution.

6. Towards setting experimental parameters with informed decisions via modeling

Computational modeling applied to bioprinting may prove extremely useful in improving the throughput, resolution, and viability of bioprinting. In order to optimize these factors in droplet-based printing, it is of utmost importance to understand the dependence of cell viability on droplet impact. In other words, modeling of droplet impact can be utilized to determine appropriate experimental parameters to preserve post-printing cell viability. Parameters pertinent to droplet impact modeling include droplet size, velocity upon impact, and material properties. Hendriks et al. introduced a model to describe cell viability as a function cell-encapsulating droplet size, viscosity of the droplet, and the impact velocity [14]. The proposed model was also verified experimentally by cell spray experiments. As opposed to the relatively narrow impact parameter space of drop-on-demand printing, spray deposition allows for a much large range of impact parameters [51,53,114–117]. Additionally, cell viability post-spraying can be controlled, due to the significant influence of spray parameters on post-impact cell viability, to study the effect of different parameters [15,118–120]. Furthermore, the shear stress exerted on the cell is much lower during spraying than during impact, so the results are highly dependent on impact and less so on the droplet deposition method. In the experiments, droplet size and impact velocity was measured to determine the corresponding model predictions, while cell viability was assessed as a function of air pressure, liquid viscosity, the distance from droplet formation to impact, and the stiffness of the receiving substrate [14]. Fig. 8 provides a graphical overview of the described experimental protocol and the key variable describing the cell-containing droplets.

The model used by Hendriks et al. relied on the deformation and elongation of the cell membrane. The cell membrane may increase in area up to approximately five-percent without cell death, whereas larger elongation can cause rupture in the cell membrane, and therefore cell death. The probability of survival was modeled as a function of the relative cell membrane area, representative of the elongation of the cell membrane [14]. Here, the base case was a cell impact on a hard surface when the cell was considered a spherical Newtonian liquid droplet with diameter D_c and velocity V_c (Fig. 8C, D), viscosity μ_c = 12 mPa s, density ρ_c = 1015 kg/m^3, and surface tension σ_c = 0.072 N/m^2. The maximum spreading diameter was calculated as a function of the Weber number, defined as the ratio of kinetic and surface energy [121–123]. The resulting shape of the cell was defined by assuming cell deformation into an oblate spheroid and volume conservation [14]. The model also factored in the stiffness of the impact surface, where a liquid pool of equal material properties to the droplet is considered the soft surface limit. A droplet impacting such a soft surface may be approximated as a droplet of twice the diameter and half the velocity impacting a hard surface [124]. The results from the described model are shown in Fig. 9. The viability probability of individual cells as a function of impact velocity for different sizes of the encapsulating droplet (Fig. 9A) shows that at low velocities, the cell viability is loosely dependent on the impact parameters due to the fact that cell deformation is assumed to be small and constant for low Weber numbers [14]. As velocity (and thus the Weber number) increases, cell viability decreases. Furthermore, the size and viscosity of the encapsulating droplet has a strong effect on cell viability at greater velocities. Larger surrounding droplets provide greater cushioning and thereby improve viability, while greater viscosity negatively affects cell viability. The effect of droplet viscosity is plotted in Fig. 9B

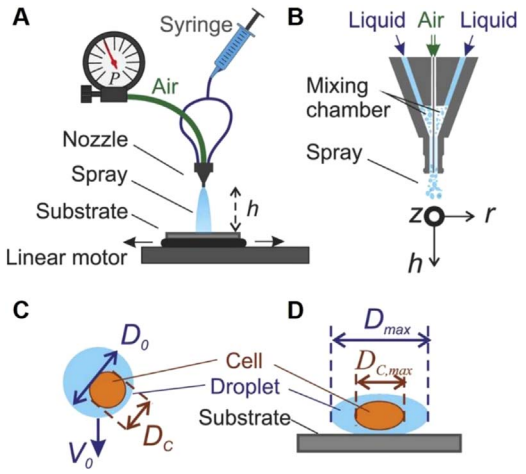

Fig. 8. Overview of analytical model for cell viability after impact [14]. (A) A two-phase spray nozzle, positioned a distance h from the surface, generates spray. Cell-laden liquid of viscosity μ is delivered to the nozzle using by a syringe pump. Air at controlled pressure P is applied to the nozzle gas inlet. The receiving substrate is moved horizontally by a linear motor to ensure homogeneous impact. (B) Cross-section of the nozzle depicting the flow of air and liquid with indication of the coordinate system. (C, D) Key variables and dimensions describing cell-encapsulating droplets for a droplet (C) in air and (D) during impact. Reproduced, with permission, from [14].

[14]. As viscosity increases, cell death is more likely to occur since deformation of the cell-containing droplet primarily occurs within the cell itself, thereby stretching the cell membrane. Another factor considered by this model is the distance between the nozzle and substrate: as the distance increases, the probability of viability also increases due to the droplet velocity decreasing far from the nozzle. A final conclusion was that decreasing the surface stiffness improve viability by offering more cushioning during impact. The results of this model are summarized in Fig. 9C, which shows viability as a function of both droplet size and speed, while also considering the influence of pressure and distance from the nozzle [14].

Another important factor in optimizing printing resolution and viability is the shear stress that occurs during 3D-bioprinting. Bioprinting involves a combination of mechanical and thermal stresses which can adversely affect cell viability and behavior post-printing [14,45,93,108]. As investigated by Blaeser et al., shear stress is of particular interest and concern, as it is unavoidable during any sort of dispensing process and should be considered for any and all forms of printing methods [125]. The level of shear stress inflicted upon the printing medium is directly affected by printing parameters including nozzle diameter, applied pressure, and viscosity of the medium [93,108]. Shear stress is an important consideration in bioprinting since different levels of shear stress can have varying impacts on cell behavior. For instance, moderate shear stress can influence stem cell differentiation, while excessive shear stress can disrupt cell membranes and be damaging [126]. During the process of bioprinting, the medium, which is often of high viscosity, is forced through a small orifice; however, Blaeser et al. showed that as viscosity increases and nozzle diameter decreases, while printing resolution improves, it is at the cost of greater shear stress. Accordingly, a micro-valve-based bioprinter, coupled with a straightforward fluid dynamic model, was used to test

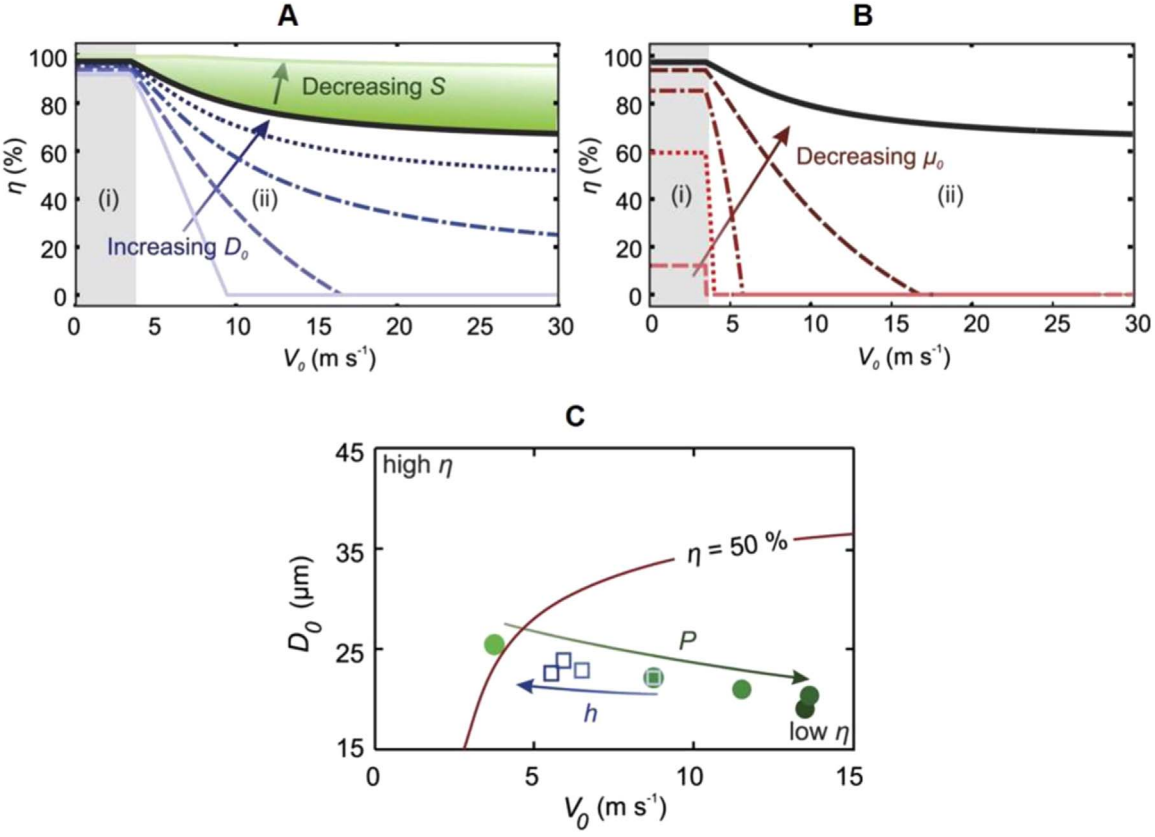

Fig. 9. Cell survival as a function of impact velocity, droplet viscosity, and droplet size and speed [14]. (A) Influence of droplet diameter (indicated by lines for $\frac{D_0}{D_c}$ = 1, 1.5, 2, 2.5, and 3) and surface stiffness (indicated by color gradient where S = 1 is stiff and S = 0 is liquid). (B) Influence of droplet viscosity (lines plotted for μ_0 = 1, 2, 4, 8, and 12 mPa s). Solid black line represents viability values for reference parameters of $\frac{D_0}{D_c}$ = 3, $\frac{\mu_c}{\mu_0}$ = 10, and S = 1. Within the shaded Region (i), indicating low-Weber number regime (We < 5), cell deformation is small and independent of impact velocity. Within Region (ii), viability decreases with increasing velocity due to increasing cell deformation. (C) Influence of droplet size and speed on cell viability. Dots indicate mean diameter versus mean velocity as a function of spray pressure (arrow represents increasing pressure from 0.2•10^5 to 1•10^5 Pa). Squares indicate distance from nozzle (for 30 to 150 mm). As pressure increases, droplet size decreases and impact velocity increases, thereby reducing viability. Reproduced, with permission, from [14].

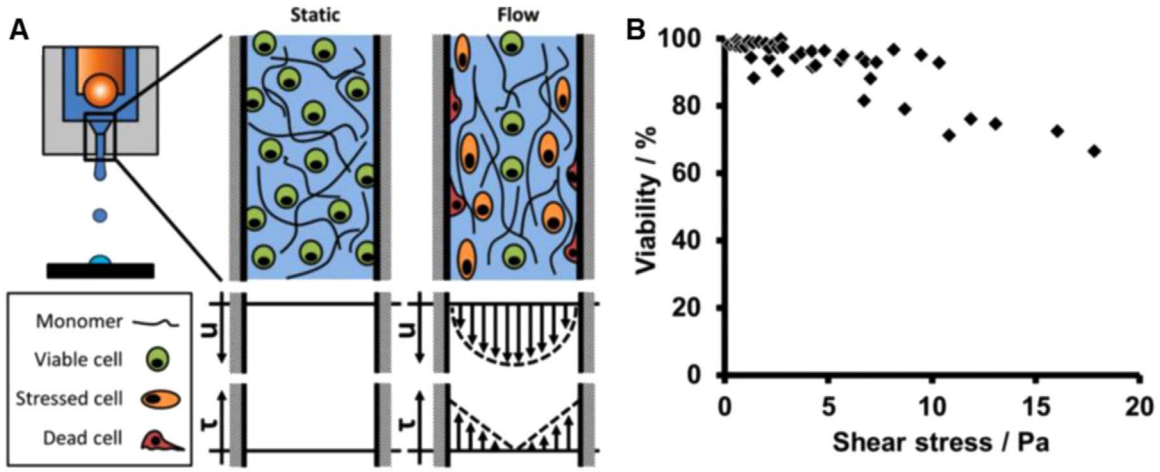

Fig. 10. Effect of shear stress during the bioprinting process on cell viability [125]. (A) Schematic illustration of the velocity (μ) and shear stress (τ) distribution of the cell-laden hydrogel as it passes through the nozzle of a micro-valve bioprinter. Within the nozzle, the effect of the shear stress on the viability of the cells is illustrated, showing greater cell damage closer to the walls of the nozzle. (B) Plot of cell viability versus shear stress, demonstrating a decrease in viability as the level of shear stress increases. Reproduced, with permission, from [125].

the hypothesis that regulating shear stress can prove beneficial in achieving the balance between cell integrity and printing resolution. A micro-valve bioprinter was used such that single droplets of cell-laden hydrogel were dispensed. As droplets were formed, the cells were exposure primarily to shear stress as the hydrogel flowed through the valves (Fig. 10).

The computational fluid dynamics model for the transient flow of non-Newtonian fluids used by Blaeser et al. was based on the Bernoulli equation for unsteady flow, the law of Hagen-Poisseuille, and the Ostwald-de Waele relationship, also known as the Power-law [125]. These three equations were then transformed into a non-linear, first-order differential equation to describe the flow of hydrogel through the micro-valve. The equation, resultingly, considered the effects of wall-friction and shear stress. The equation was solved numerically in order to calculate the average drop speed, drop volume, and shear stress occurring within the valve as a function of nozzle diameter and length and hydrogel viscosity [125]. To validate these calculated results, alginate was selected as the experimental material, chosen for its shear-thinning behavior [127,128]. The viscosity and power-law constants (K and n) were measured using a dynamic sear rheometer for three different concentrations of alginate solutions (0.5, 1.0, 1.5$\frac{wt}{v}$%) each with three different cell concentrations (0, 1, and 10 million cells per milliliter) (Fig. 11A–C). As the cell number increased, the flow consistency index (K) increased, the flow behavior index (n) decreased, and the viscosity decreased; however, the effective viscosity increased while amplifying the shear thinning effect [125]. Additionally, the drop volume and speed were measured and compared to the calculated values (Fig. 11D–F). A minimal speed, the tear-off speed, required to form a single drop was experimentally determined and was in agreement with previously reported results on the drop kinetics of inkjet printers [46,129,130]. With the validated results, the shear stress and drop volume were able to be plotted against the drop speed, showing a strong influence of nozzle size on both shear stress and drop volume (Fig. 11G–I). Namely, larger valves result in lower shear stress at the expense of larger drops [125]. The effect of shear stress on viability was finally studied and classified into three groups: <5 kPa, 5 − 10 kPa, and >10 kPa. Viability of cells exposed to the lowest range of shear stress was almost unaffected by the printing process (96% viability) while the higher shear stress ranges resulted in more significant losses in viability (91% and 76% viability, respectively) [125]. In general, short-time exposure to high levels of shear stress has an immediate and detrimental effect on cells and can negatively affect the long-term proliferation as well. With this in mind, the nozzle diameter and pressure were selectively tuned to yield a drop speed very close to the minimum tear-off speed without causing excessive shear stress. Ultimately, the results of these experiments and the applied computational model demonstrated the capability of high-resolution, low-shear stress bioprinting by careful and purposeful selection of printing parameters, namely the viscosity of the printing medium, nozzle diameter, and applied pressure, and consequently the drop speed.

7. Post-printing: fusion of printed constructs

Another important component of the bioprinting process is what happens after the bioprinter has deposited cell-laden bioink. Whether a droplet-based or extrusion-based bioprinter, it deposits bioink in a layer-by-layer fashion. Over time, cells within the printed material proliferate and grow, and eventually the layers fuse into a single, solid form. For droplet-based bioprinting, this self-assembly goes a step further, as multicellular droplets must self-assemble. To aid in this growth and fusion, the printed forms may be placed into a bioreactor, facilitating the fusion process of self-assembly, maturation, and differentiation [131]. For this crucial fusion step in the bioprinting process, computational modeling can be used to model the fusion of cellular aggregates in biofabrication. Various mathematical methods can be applied for this purpose.

Utilizing a method often used to simulate the time evolution of a process that occur with known transition rates among states, Sun and Wang studied cell self-assembly and cellular aggregate fusion of multicellular aggregate systems using kinetic Monte Carlo (KMC) methods [132]. KMC was used to predict the time evolution of post-printing morphological structure formation during morphogenesis of tissues. Specifically, a discrete, multicellular lattice model, which describes the interaction between cells based on a differential adhesion hypothesis, was used to predict equilibrium tissue configurations based on the interfacial tensions between different cell populations that compose the bioprinted tissue (these interfacial tensions depend on the adhesion between cells) [133–135]. In order to address how configurations develop over time, the lattice model was implemented in a list-based KMC algorithm to simulate the fusion of single-cell type tissues in various geometries, including a ring, a sheet, and a tube [136–138]. Additionally, the KMC model was employed to study the process of cell sorting during the fusion of cellular aggregates of multiple cell types with varying degrees of adhesion and compatibility.

An alternative mathematical model was developed by Yang et al. who modeled the fusion of cellular aggregates in biofabrication using phase field theories. In particular, Yang et al. formulated a model which considers the chemical-mechanical interactions of the cellular aggre-

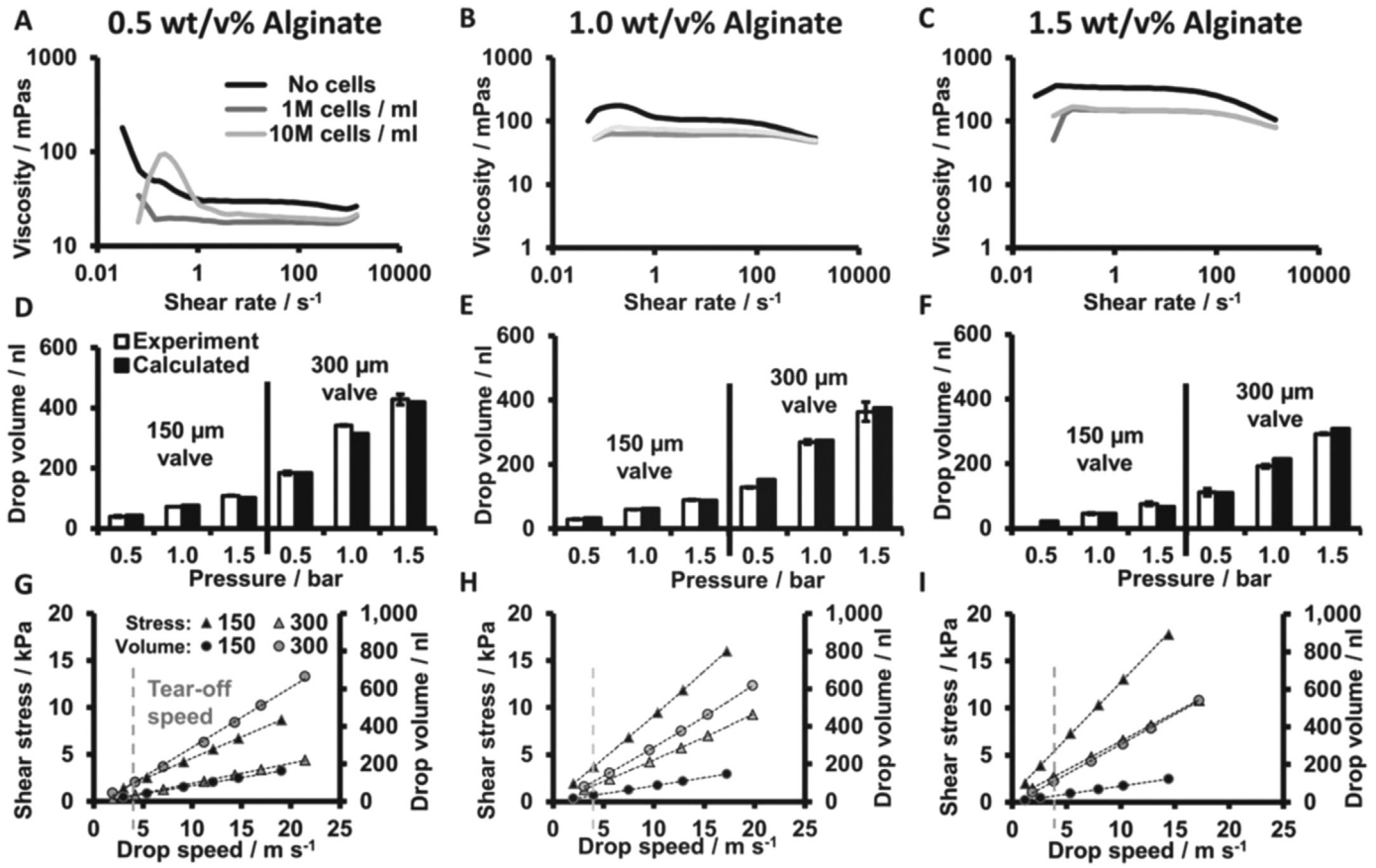

Fig. 11. Experimental and computational viscosity, drop volume, drop speed, and shear stress results for droplet-based bioprinting [125]. (A–C) Rheological characterization of alginate hydrogels with and without cells. (D–F) Validation of computational fluid dynamic model by comparison to experimental results for drop volume using different applied pressure and different nozzle diameters. For all alginate solutions, drop volume consistently increased with increasing pressure. (G–I) Plot of shear stress and drop volume versus drop speed. For all alginate solutions, shear stress and drop volume increased as drop speed increased. The minimum tear-off speed is indicated by the dotted vertical line. Results show that shear stress and drop volume can be selectively minimized to improve both viability and resolution. Reproduced, with permission, from [125].

gates [131,139–141]. To this end, the cellular aggregates and the surrounding hydrogel were modeled as a spheroid of complex fluids and a viscous fluid, respectively. The aggregate and surrounding fluid may then be considered a binary fluid mixture of two immiscible complex fluids. A mean-field potential was then developed, integrating both the long-range, attractive interactions between cells, as well as the short-range, repulsive interactions due to the assumed immiscibility. The phase field model was then implemented using a higher order spectral method to simulate the formation of fundamental geometries, such as a ring, a sheet of tissues, and a y-shaped bifurcating vascular junction, each geometry being comprised of layers of spheroidal cellular clusters (Fig. 12) [131].

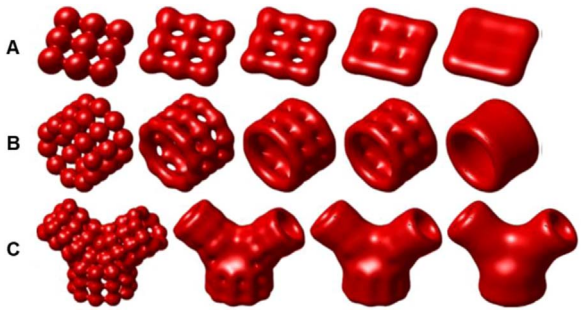

Fig. 12. Fusion of cellular aggregates modeled by phase field theories [131]. Fusion of cellular aggregates into various geometrical forms, including: (A) a sheet, (B) a ring, and (C) a y-shaped junction. Snapshots are taken at the following time steps, relative to a characteristic time scale determined by the growth time scale of the interface and the cellular cluster fusion time scale: (A) 0, 0.5, 1, 2, and 3; (B) 0, 0.1, 0.24, 0.25, and 0.5; and (C) 0, 0.2, 0.3, and 0.5. Reproduced, with permission, from [131].

8. Conclusions and future directions

Bioprinting is a maturing field, harnessing the benefits and capabilities of additive manufacturing for biomedical applications. Three-dimensional bioprinting allows for the direct fabrication of biomimetic tissues by depositing individual layers of biomaterial. This ability to fabricate realistic tissues has been utilized in several applications in tissue engineering and regenerative medicine. While experimental work is useful in testing new bioprinting platforms and biomaterials, it cannot sustain the rapidly growing trajectory of the field. Computational modeling enhances the ability to investigate the bioprinting process from many different standpoints, offering an alternative method for studying and advancing the capabilities of three-dimensional bioprinting. In particular, computational modeling should be utilized to address the major limitations of bioprinting: post-printing viability and printing resolution. For improving viability of bioprinted tissues, numerical methods can be implemented to study the impact dynamics of encapsulated cells as they are deposited, allowing researchers to determine the deformation of the encapsulated cell and the rate of deformation, which, among other factors, depend on viscoelastic features, droplet size, and velocity. Modeling can help to reveal how various parameters affect post-printing viability without the need for entirely new experiments. Furthermore, computational models can also be utilized to optimize filament integrity in extrusion-based bioprinting.

The significance of computational models applied to bioprinting cannot, and should not, be understated: analytical models describing

cell viability as a function of droplet impact parameters can be used not only to predict cell-viability trends, but also be applied to determine appropriate printing parameters. The numerical models presented provide a framework for optimizing cell viability in future bioprinting applications. As bioprinting forges ahead, high-throughput and high-resolution fabrication of 3D tissue constructs will require tools for preserving cell viability, even for more fragile cell types or high-viscosity bioinks. For droplet-based bioprinting, parameters such as the droplet diameter, the viscosity of the bioink droplets, the distance from nozzle-to-substrate, and thus the impact velocity, and the stiffness of the substrate can be manipulated to yield optimum cell viability, based on computational model results. Likewise, the resolution and structural integrity of extrusion-based printing can be optimized by numerical simulation of filaments based on material properties and geometrical parameters.

The future of three-dimensional bioprinting is dependent on the ability to improve the viability and resolution. Future work may look into resolving some of the underlying assumptions and remaining gaps in current models. For instance, some models discussed assume cells are centered within the droplet; however, in larger volume droplets, cell may be located at the edge of the spreading film where shear stresses are higher than in the center. Also, for larger droplet volumes, the number of cells per drop would likely increase. The effect of viscoelastic behavior of cell and encapsulating droplets should be more extensively studied. Additionally, there remains a gap in computational models for the shape fidelity of droplet-based bioprinting schemes. Creating more encompassing models, ones which address these remaining areas for improvement, will prove even more impactful in setting experimental parameters with informed decisions from modeling.

Acknowledgements

S.T. acknowledges the American Heart Association Scientist Development Grant (15SDG25080056), Connecticut Innovations Biopipeline Award, and the University of Connecticut Research Excellence Program award for financial support of this research. E.L. acknowledges the NASA Connecticut Space Grant Consortium for the Undergraduate Research Fellowship Grant (P-1175, NNH16ZHA002C). M.M. is supported by the Scientific and Technical Research Council of Turkey (TUBITAK) under Grant number 115M688.

References

[1] S.V. Murphy, A. Atala, 3D bioprinting of tissues and organs, Nat. Biotechnol. 32 (2014) 773–785. http://dx.doi.org/10.1038/nbt.2958.
[2] S. Knowlton, S. Tasoglu, A bioprinted liver-on-a-chip for drug screening applications, Trends Biotechnol. 34 (2016) 681–682. http://dx.doi.org/10.1016/j.tibtech.2016.05.014.
[3] S. Knowlton, B. Yenilmez, S. Tasoglu, Towards single-step biofabrication of organs on a chip via 3D printing, Trends Biotechnol. 34 (2016) 685–688. http://dx.doi.org/10.1016/j.tibtech.2016.06.005.
[4] H. Lee, D.-W. Cho, One-step fabrication of an organ-on-a-chip with spatial heterogeneity using a 3D bioprinting technology, Lab Chip 16 (2016) 2618–2625. http://dx.doi.org/10.1039/C6LC00450D.
[5] S. Knowlton, A. Joshi, B. Yenilmez, I.T. Ozbolat, C.K. Chua, A. Khademhosseini, S. Tasoglu, Advancing cancer research using bioprinting for tumor-on-a-chip platforms, Int. J. Bioprint. 2 (2016) 3–8. http://dx.doi.org/10.18063/IJB.2016.02.003.
[6] S. Knowlton, S. Onal, C.H. Yu, J.J. Zhao, S. Tasoglu, Bioprinting for cancer research, Trends Biotechnol. 33 (2015) 504–513. http://dx.doi.org/10.1016/j.tibtech.2015.06.007.
[7] X. Dai, C. Ma, Q. Lan, T. Xu, 3D bioprinted glioma stem cells for brain tumor model and applications of drug susceptibility, Biofabrication 8 (2016). http://dx.doi.org/10.1088/1758-5090/8/4/045005.
[8] Y.S. Zhang, M. Duchamp, R. Oklu, L.W. Ellisen, R. Langer, A. Khademhosseini, Bioprinting the cancer microenvironment, ACS Biomater. Sci. Eng. 2 (2016) 1710–1721. http://dx.doi.org/10.1021/acsbiomaterials.6b00246.
[9] C. Mandrycky, Z. Wang, K. Kim, D.H. Kim, 3D bioprinting for engineering complex tissues, Biotechnol. Adv. 34 (2016) 422–434. http://dx.doi.org/10.1016/j.biotechadv.2015.12.011.
[10] P. Bajaj, R.M. Schweller, A. Khademhosseini, J.L. West, R. Bashir, 3D biofabrication strategies for tissue engineering and regenerative medicine, Annu. Rev. Biomed. Eng. 16 (2014) 247–276. http://dx.doi.org/10.1146/annurev-bioeng-071813-105155.
[11] G. Gao, X. Cui, Three-dimensional bioprinting in tissue engineering and regenerative medicine, Biotechnol. Lett. 38 (2016) 203–211. http://dx.doi.org/10.1007/s10529-015-1975-1.
[12] I.T. Ozbolat, Bioprinting scale-up tissue and organ constructs for transplantation, Trends Biotechnol. 33 (2015) 395–400. http://dx.doi.org/10.1016/j.tibtech.2015.04.005.
[13] S. Tasoglu, U. Demirci, Bioprinting for stem cell research, Trends Biotechnol. 31 (2013) 10–19. http://dx.doi.org/10.1016/j.tibtech.2012.10.005.
[14] J. Hendriks, C. Willem Visser, S. Henke, J. Leijten, D.B.F. Saris, C. Sun, D. Lohse, M. Karperien, Optimizing cell viability in droplet-based cell deposition, Sci. Rep. 5 (2015) 1–10. http://dx.doi.org/10.1038/srep11304.
[15] S. Tasoglu, G. Kaynak, A.J. Szeri, U. Demirci, M. Muradoglu, Impact of a compound droplet on a flat surface: a model for single cell epitaxy, Phys. Fluids 22 (2010) 082103. http://dx.doi.org/10.1063/1.3475527.
[16] H. Gudapati, M. Dey, I. Ozbolat, A comprehensive review on droplet-based bioprinting: past, present and future, Biomaterials 102 (2016).
[17] E. Lepowsky, S. Tasoglu, 3D printing for drug manufacturing: a perspective on the future of pharmaceuticals, Int. J. Bioprint. 4 (2018) 119.
[18] T. Billiet, M. Vandenhaute, J. Schelfhout, S. Van Vlierberghe, P. Dubruel, A review of trends and limitations in hydrogel-rapid prototyping for tissue engineering, Biomaterials 33 (2012) 6020–6041. http://dx.doi.org/10.1016/j.biomaterials.2012.04.050.
[19] W.-Y. Yeong, C.-K. Chua, K.-F. Leong, M. Chandrasekaran, Rapid prototyping in tissue engineering: challenges and potential, Trends Biotechnol. 22 (2004) 643–652. http://dx.doi.org/10.1016/j.tibtech.2004.10.004.
[20] R.D. Gates, G. Baghdasarian, L. Muscatine, Temperature stress causes host-cell detachment in symbiotic Cnidarians: implications for coral bleaching, Biol. Bull. 182 (1992) 324–332. http://dx.doi.org/10.2307/1542252.
[21] T. Billiet, E. Gevaert, T. De Schryver, M. Cornelissen, P. Dubruel, The 3D printing of gelatin methacrylamide cell-laden tissue-engineered constructs with high cell viability, Biomaterials 35 (2014) 49–62. http://dx.doi.org/10.1016/j.biomaterials.2013.09.078.
[22] Y. Luo, A. Lode, A.R. Akkineni, M. Gelinsky, Concentrated gelatin/alginate composites for fabrication of predesigned scaffolds with a favorable cell response by 3D plotting, RSC Adv. 5 (2015) 43480–43488. http://dx.doi.org/10.1039/C5RA04308E.
[23] A.R. Akkineni, Y. Luo, M. Schumacher, B. Nies, A. Lode, M. Gelinsky, 3D plotting of growth factor loaded calcium phosphate cement scaffolds, Acta Biomater. 27 (2015) 264–274. http://dx.doi.org/10.1016/j.actbio.2015.08.036.
[24] P. Yilgor, R.A. Sousa, R.L. Reis, N. Hasirci, V. Hasirci, 3D plotted PCL scaffolds for stem cell based bone tissue engineering, Macromol. Symp. 269 (2008) 92–99. http://dx.doi.org/10.1002/masy.200850911.
[25] R. Landers, R. Mülhaupt, Desktop manufacturing of complex objects, prototypes and biomedical scaffolds by means of computer-assisted design combined with computer-guided 3D plotting of polymers and reactive oligomers, Macromol. Mater. Eng. 282 (2000) 17–21. http://dx.doi.org/10.1002/1439-2054(20001001)282:1<17::AID-MAME17>3.0.CO;2-8.
[26] J.E. Smay, J. Cesarano, J.A. Lewis, J.C. Iii, Colloidal inks for directed assembly of 3-D periodic structures, East 18 (2002) 5429–5437. http://dx.doi.org/10.1021/la0257135.
[27] B.Y. Ahn, E.B. Duoss, M.J. Motala, X. Guo, S. Il Park, Y. Xiong, J. Yoon, R.G. Nuzzo, J.A. Rogers, J.A. Lewis, Omnidirectional printing of flexible, stretchable, and spanning silver microelectrodes, Science 323 (80) (2009) 1590–1593. http://dx.doi.org/10.1126/science.1168375.
[28] G. Vozzi, C. Flaim, A. Ahluwalia, S. Bhatia, Fabrication of PLGA scaffolds using soft lithography and microsyringe deposition, Biomaterials 24 (2003) 2533–2540. http://dx.doi.org/10.1016/S0142-9612(03)00052-8.
[29] G. Vozzi, A. Previti, D. De Rossi, A. Ahluwalia, Microsyringe-based deposition of two-dimensional and three-dimensional polymer scaffolds with a well-defined geometry for application to tissue engineering, Tissue Eng. 8 (2002) 1089–1098. http://dx.doi.org/10.1089/107632702320934182.
[30] G. Tartarisco, G. Gallone, F. Carpi, G. Vozzi, Polyurethane unimorph bender microfabricated with pressure assisted microsyringe (PAM) for biomedical applications, Mater. Sci. Eng. C 29 (2009) 1835–1841. http://dx.doi.org/10.1016/j.msec.2009.02.017.
[31] Z. Xiong, Y. Yan, S. Wang, R. Zhang, C. Zhang, Fabrication of porous scaffolds for bone tissue engineering via low-temperature deposition, Scr. Mater. 46 (2002) 771–776. http://dx.doi.org/10.1016/S1359-6462(02)00071-4.
[32] L. Liu, Z. Xiong, R. Zhang, L. Jin, Y. Yan, A novel osteochondral scaffold fabricated via multi-nozzle low-temperature deposition manufacturing, J. Bioact. Compat. Polym. 24 (2009) 18–30. http://dx.doi.org/10.1177/0883911509102347.
[33] J. Cesarano, A review of robocasting technology, MRS Proc. 542 (2011) 133–139. http://dx.doi.org/10.1557/PROC-542-133.
[34] N.G. Durmus, S. Tasoglu, U. Demirci, Bioprinting: functional droplet networks, Nat. Mater. 12 (2013) 478–479. http://dx.doi.org/10.1038/nmat3665.
[35] U. Demirci, G. Montesano, Single cell epitaxy by acoustic picolitre droplets, Lab Chip 7 (2007) 1139. http://dx.doi.org/10.1039/b704965j.
[36] U. Demirci, Acoustic picoliter droplets for emerging applications in semiconductor industry and biotechnology, J. Micro. Syst. 15 (2006) 957–966. http://dx.doi.org/10.1109/JMEMS.2006.878879.
[37] C.H. Droplets, S. Moon, D. Ph, S.K. Hasan, Y.S. Song, D. Ph, Layer by Layer Three-Dimensional Tissue, 16, 2010.
[38] A. Faulkner-Jones, S. Greenhough, J.A. King, J. Gardner, A. Courtney, W. Shu, Development of a valve-based cell printer for the formation of human embryonic stem cell spheroid aggregates, Biofabrication 5 (2013). http://dx.doi.org/10.1088/1758-5082/5/1/015013.
[39] W. Lee, J.C. Debasitis, V.K. Lee, J.H. Lee, K. Fischer, K. Edminster, J.K. Park, S.S. Yoo, Multi-layered culture of human skin fibroblasts and keratinocytes through three-dimensional freeform fabrication, Biomaterials 30 (2009) 1587–1595. http://dx.doi.org/10.1016/j.biomaterials.2008.12.009.

[40] A. Faulkner-Jones, C. Fyfe, D.-J. Cornelissen, J. Gardner, J. King, A. Courtney, W. Shu, Bioprinting of human pluripotent stem cells and their directed differentiation into hepatocyte-like cells for the generation of mini-livers in 3D, Biofabrication 7 (2015) 44102. http://dx.doi.org/10.1088/1758-5090/7/4/044102.

[41] B. Derby, Bioprinting: inkjet printing proteins and hybrid cell-containing materials and structures, J. Mater. Chem. 18 (2008) 5717. http://dx.doi.org/10.1039/b807560c.

[42] Lord Rayleigh, On the instability of jets, Proc. Lond. Math. Soc. s1–10 (1878) 4–13.

[43] T. Xu, J. Jin, C. Gregory, J.J. Hickman, T. Boland, Inkjet printing of viable mammalian cells, Biomaterials 26 (2005) 93–99. http://dx.doi.org/10.1016/j.biomaterials.2004.04.011.

[44] T. Boland, T. Xu, B. Damon, X. Cui, Application of inkjet printing to tissue engineering, Biotechnol. J. 1 (2006) 910–917. http://dx.doi.org/10.1002/biot.200600081.

[45] X. Cui, D. Dean, Z.M. Ruggeri, T. Boland, Cell damage evaluation of thermal inkjet printed chinese hamster ovary cells, Biotechnol. Bioeng. 106 (2010) 963–969. http://dx.doi.org/10.1002/bit.22762.

[46] H. Wijshoff, The dynamics of the piezo inkjet printhead operation, Phys. Rep. 491 (2010) 77–177. http://dx.doi.org/10.1016/j.physrep.2010.03.003.

[47] M. Singh, H.M. Haverinen, P. Dhagat, G.E. Jabbour, Inkjet printing-process and its applications, Adv. Mater. 22 (2010) 673–685. http://dx.doi.org/10.1002/adma.200901141.

[48] C. Xu, W. Chai, Y. Huang, R.R. Markwald, Scaffold-free inkjet printing of three-dimensional zigzag cellular tubes, Biotechnol. Bioeng. 109 (2012) 3152–3160. http://dx.doi.org/10.1002/bit.24591.

[49] K. Christensen, C. Xu, W. Chai, Z. Zhang, J. Fu, Y. Huang, Freeform inkjet printing of cellular structures with bifurcations, Biotechnol. Bioeng. 112 (2015) 1047–1055. http://dx.doi.org/10.1002/bit.25501.

[50] K. Pataky, T. Braschler, A. Negro, P. Renaud, M.P. Lutolf, J. Brugger, Microdrop printing of hydrogel bioinks into 3D tissue-like geometries, Adv. Mater. 24 (2012) 391–396. http://dx.doi.org/10.1002/adma.201102800.

[51] S. Yamaguchi, A. Ueno, Y. Akiyama, K. Morishima, Cell patterning through inkjet printing of one cell per droplet, Biofabrication 4 (2012). http://dx.doi.org/10.1088/1758-5082/4/4/045005.

[52] S. Kamisuki, T. Hagata, C. Tezuka, Y. Nose, M. Fujii, M. Atobe, A low power, small, electrostatically-driven commercial inkjet head, in: Proc. MEMS 98. IEEE. Elev. Annu. Int. Work. Micro Electro Mech. Syst. An Investig. Micro Struct. Sensors, Actuators, Mach. Syst. (Cat. No.98CH36176). 1998, pp. 63–68. ⟨http://dx.doi.org/10.1109/MEMSYS.1998.659730⟩.

[53] Y. Nishiyama, M. Nakamura, C. Henmi, K. Yamaguchi, S. Mochizuki, H. Nakagawa, K. Takiura, Development of a three-dimensional bioprinter: construction of cell supporting structures using hydrogel and state-of-the-art inkjet technology, J. Biomech. Eng. 131 (2009) 35001. http://dx.doi.org/10.1115/1.3002759.

[54] M.S. Onses, E. Sutanto, P.M. Ferreira, A.G. Alleyne, J.A. Rogers, Mechanisms, capabilities, and applications of high-resolution electrohydrodynamic jet printing, Small 11 (2015) 4237–4266. http://dx.doi.org/10.1002/smll.201500593.

[55] L. Gasperini, D. Maniglio, A. Motta, C. Migliaresi, An electrohydrodynamic bioprinter for alginate hydrogels containing living cells, Tissue Eng. Part C Methods 21 (2015) 123–132. http://dx.doi.org/10.1089/ten.tec.2014.0149.

[56] M.J. Poellmann, K.L. Barton, S. Mishra, A.J.W. Johnson, Patterned hydrogel substrates for cell culture with electrohydrodynamic jet printing, Macromol. Biosci. 11 (2011) 1164–1168. http://dx.doi.org/10.1002/mabi.201100004.

[57] E. Sutanto, K. Shigeta, Y.K. Kim, P.G. Graf, D.J. Hoelzle, K.L. Barton, A.G. Alleyne, P.M. Ferreira, J.A. Rogers, A multimaterial electrohydrodynamic jet (E-jet) printing system, J. Micromech. Microeng. 22 (2012). http://dx.doi.org/10.1088/0960-1317/22/4/045008.

[58] I. Hayati, A.I. Bailey, T.F. Tadros, Mechanism of stable jet formation in electrohydrodynamic atomization, Nature 319 (1986) 41–43. http://dx.doi.org/10.1038/324148a0.

[59] H.S. Kim, D.Y. Lee, J.H. Park, J.H. Kim, J.H. Hwang, H.I. Jung, Optimization of electrohydrodynamic writing technique to print collagen, Exp. Tech. 31 (2007) 15–19. http://dx.doi.org/10.1111/j.1747-1567.2007.00154.x.

[60] V.L. Workman, L.B. Tezera, P.T. Elkington, S.N. Jayasinghe, Controlled generation of microspheres incorporating extracellular matrix fibrils for three-dimensional cell culture, Adv. Funct. Mater. 24 (2014) 2648–2657. http://dx.doi.org/10.1002/adfm.201303891.

[61] S.N. Jayasinghe, A.N. Qureshi, P.A.M. Eagles, Electrohydrodynamic jet processing: an advanced electric-field-driven jetting phenomenon for processing living cells, Small 2 (2006) 216–219. http://dx.doi.org/10.1002/smll.200500291.

[62] J. Pardeike, D.M. Strohmeier, N. Schrödl, C. Voura, M. Gruber, J.G. Khinast, A. Zimmer, Nanosuspensions as advanced printing ink for accurate dosing of poorly soluble drugs in personalized medicines, Int. J. Pharm. 420 (2011) 93–100. http://dx.doi.org/10.1016/j.ijpharm.2011.08.033.

[63] J. Goole, K. Amighi, 3D printing in pharmaceutics: a new tool for designing customized drug delivery systems, Int. J. Pharm. 499 (2016) 376–394. http://dx.doi.org/10.1016/j.ijpharm.2015.12.071.

[64] M. Sokolsky-Papkov, K. Agashi, A. Olaye, K. Shakesheff, A.J. Domb, J. Lam, S. Lu, F.K. Kasper, A.G. Mikos, Polymer carriers for drug delivery in tissue engineering, Adv. Drug Deliv. Rev. 59 (2014) 187–206. http://dx.doi.org/10.1016/j.addr.2007.04.001.

[65] B. Leukers, H. Gülkan, S. Irsen, S. Milz, Hydroxyapatite scaffolds for bone tissue engineering made by 3D printing, J. Mater. Sci.: Mater. Med. 6 (2005) 1121–1124. http://dx.doi.org/10.1007/s10856-005-4716-5.

[66] F. Badalà, K. Nouri-mahdavi, D.A. Raoof, 3D printing of composite calcium phosphate and collagen scaffolds for bone regeneration, Computer 144 (2008) 724–732. http://dx.doi.org/10.1038/jid.2014.371.

[67] A. Levy, A. Miriyev, A. Elliott, S.S. Babu, N. Frage, Additive manufacturing of complex-shaped graded TiC/steel composites, Mater. Des. 118 (2017) 198–203. http://dx.doi.org/10.1016/j.matdes.2017.01.024.

[68] A. Pfister, Landers, A. Laib, R. Schmelzeisen, Biofunctional rapid prototyping for tissue engineering applications: 3D bioplotting versus 3D printing, J. Polym. Sci. Part A Polym. Chem. 42 (2003) 624–638. http://dx.doi.org/10.1002/pola.10807.

[69] T. Boland, X. Tao, B.J. Damon, B. Manley, P. Kesari, S. Jalota, S. Bhaduri, Drop-on-demand printing of cells and materials for designer tissue constructs, Mater. Sci. Eng. C 27 (2007) 372–376. http://dx.doi.org/10.1016/j.msec.2006.05.047.

[70] S. Knowlton, S. Anand, T. Shah, S. Tasoglu, Bioprinting for neural tissue engineering, Trends Neurosci. 41 (2018) 31–46. http://dx.doi.org/10.1016/j.tins.2017.11.001.

[71] K.C. Hribar, P. Soman, J. Warner, P. Chung, S. Chen, Light-assisted direct-write of 3D functional biomaterials, Lab Chip 14 (2014) 268–275. http://dx.doi.org/10.1039/C3LC50634G.

[72] D.J. Odde, M.J. Renn, Laser-guided direct writing for applications in biotechnology, Trends Biotechnol. 17 (1999) 385–389. http://dx.doi.org/10.1016/S0167-7799(99)01355-4.

[73] D.J. Odde, M.J. Renn, Laser-guided direct writing of living cells, Biotechnol. Bioeng. 67 (2000) 312–318. http://dx.doi.org/10.1002/(SICI)1097-0290(20000205)67:3<312::AID-BIT7>3.0.CO;2-F.

[74] M.J. Renn, R. Pastel, H.J. Lewandowski, Laser guidance and trapping of mesoscale particles in hollow-core optical fibers, Phys. Rev. Lett. 82 (1999) 1574–1577. http://dx.doi.org/10.1103/PhysRevLett.82.1574.

[75] J. Xu, S.A. Grant, R.L. Pastel, Laser-guided direct writing: a novel method to deposit biomolecules for biosensors arrays, IEEE Trans. Biomed. Eng. 50 (2003) 126–128. http://dx.doi.org/10.1109/TBME.2002.805461.

[76] Y. Nahmias, R.E. Schwartz, C.M. Verfaillie, D.J. Odde, Laser-guided direct writing for three-dimensional tissue engineering, Biotechnol. Bioeng. 92 (2005) 129–136. http://dx.doi.org/10.1002/bit.20585.

[77] B.R. Ringeisen, C.M. Othon, J.A. Barron, D. Young, B.J. Spargo, Jet-based methods to print living cells, Biotechnol. J. 1 (2006) 930–948. http://dx.doi.org/10.1002/biot.200600058.

[78] I.T. Ozbolat, K.K. Moncal, H. Gudapati, Evaluation of bioprinter technologies, Addit. Manuf. 13 (2017) 179–200. http://dx.doi.org/10.1016/j.addma.2016.10.003.

[79] J.A. Barron, B.J. Spargo, B.R. Ringeisen, Biological laser printing of three dimensional cellular structures, Appl. Phys. A 79 (2004) 1027–1030. http://dx.doi.org/10.1007/s00339-004-2620-3.

[80] Y. Lin, G. Huang, Y. Huang, T. Jeremy Tzeng, D. Chrisey, Effect of laser fluence in laser-assisted direct writing of human colon cancer cell, Rapid Prototyp. J. 16 (2010) 202–208. http://dx.doi.org/10.1108/13552541011034870.

[81] L. Koch, A. Deiwick, S. Schlie, S. Michael, M. Gruene, V. Coger, D. Zychlinski, A. Schambach, K. Reimers, P.M. Vogt, B. Chichkov, Skin tissue generation by laser cell printing, Biotechnol. Bioeng. 109 (2012) 1855–1863. http://dx.doi.org/10.1002/bit.24455.

[82] S. Knowlton, B. Yenilmez, S. Anand, S. Tasoglu, Photocrosslinking-based bioprinting: examining crosslinking schemes, Bioprinting 5 (2017) 10–18. http://dx.doi.org/10.1016/j.bprint.2017.03.001.

[83] F.P.W. Melchels, J. Feijen, D.W. Grijpma, A review on stereolithography and its applications in biomedical engineering, Biomaterials 31 (2010) 6121–6130. http://dx.doi.org/10.1016/j.biomaterials.2010.04.050.

[84] J.S. Choi, H.W. Kang, I.H. Lee, T.J. Ko, D.W. Cho, Development of micro-stereolithography technology using a UV lamp and optical fiber, Int. J. Adv. Manuf. Technol. 41 (2009) 281–286. http://dx.doi.org/10.1007/s00170-008-1461-1.

[85] C. Sun, N. Fang, D.M. Wu, X. Zhang, Projection micro-stereolithography using digital micro-mirror dynamic mask, Sens. Actuators A Phys. 121 (2005) 113–120. http://dx.doi.org/10.1016/j.sna.2004.12.011.

[86] S. Maruo, K. Ikuta, Submicron stereolithography for the production of freely movable mechanisms by using single-photon polymerization, Sens. Actuators A Phys. 100 (2002) 70–76. http://dx.doi.org/10.1016/S0924-4247(02)00043-2.

[87] K.S. Lee, R.H. Kim, D.Y. Yang, S.H. Park, Advances in 3D nano/microfabrication using two-photon initiated polymerization, Prog. Polym. Sci. 33 (2008) 631–681. http://dx.doi.org/10.1016/j.progpolymsci.2008.01.001.

[88] T. Weiß, G. Hildebrand, R. Schade, K. Liefeith, Two-photon polymerization for microfabrication of three-dimensional scaffolds for tissue engineering application, Eng. Life Sci. 9 (2009) 384–390. http://dx.doi.org/10.1002/elsc.200900002.

[89] B.N. Chichkov, A. Ostendorf, Two-photon polymerization: a new approach to micromachining, Photonics Spectra 40 (2006) 72–79. http://dx.doi.org/10.1016/j.jphotochem.2006.03.004.

[90] D.W. Hutmacher, M. Sittinger, M.V. Risbud, Scaffold-based tissue engineering: rationale for computer-aided design and solid free-form fabrication systems, Trends Biotechnol. 22 (2004) 354–362. http://dx.doi.org/10.1016/j.tibtech.2004.05.005.

[91] H. Bikas, P. Stavropoulos, G. Chryssolouris, Additive manufacturing methods and modeling approaches: a critical review, Int. J. Adv. Manuf. Technol. 83 (2016) 389–405. http://dx.doi.org/10.1007/s00170-015-7576-2.

[92] T. Kamperman, S. Henke, C.W. Visser, M. Karperien, J. Leijten, Centering single cells in microgels via delayed crosslinking supports long-term 3D culture by preventing cell escape, Small 13 (2017) 1–10. http://dx.doi.org/10.1002/smll.201603711.

[93] R. Chang, J. Nam, W. Sun, Effects of dispensing pressure and nozzle diameter on cell survival from solid freeform fabrication–based direct cell writing, Tissue Eng. Part A 14 (2008) 41–48. http://dx.doi.org/10.1089/ten.a.2007.0004.

[94] Y. Yu, Y. Zhang, J.A. Martin, I.T. Ozbolat, Evaluation of cell viability and functionality in vessel-like bioprintable cell-laden tubular channels, J. Biomech. Eng. 135 (2013) 91011. http://dx.doi.org/10.1115/1.4024575.

[95] M. Li, X. Tian, D.J. Schreyer, X. Chen, Effect of needle geometry on flow rate and cell damage in the dispensing-based biofabrication process, Biotechnol. Prog. 27 (2011) 1777–1784. http://dx.doi.org/10.1002/btpr.679.

[96] A. Carlier, G.A. Skvortsov, F. Hafezi, E. Ferraris, J. Patterson, B. Koc, H. Van Oosterwyck, Computational model-informed design and bioprinting of cell-

patterned constructs for bone tissue engineering, Biofabrication 8 (2016). http://dx.doi.org/10.1088/1758-5090/8/2/025009.
[97] A. Cristea, A. Neagu, Shape changes of bioprinted tissue constructs simulated by the Lattice Boltzmann method, Comput. Biol. Med. 70 (2016) 80–87. http://dx.doi.org/10.1016/j.compbiomed.2015.12.020.
[98] S.O. Unverdi, G. Tryggvason, A front-tracking method for viscous, incompressible, multi-fluid flows, J. Comput. Phys. 100 (1992) 25–37. http://dx.doi.org/10.1016/0021-9991(92)90307-K.
[99] G. Tryggvason, B. Bunner, A. Esmaeeli, D. Juric, N. Al-Rawahi, W. Tauber, J. Han, S. Nas, Y.J. Jan, A front-tracking method for the computations of multiphase flow, J. Comput. Phys. 169 (2001) 708–759. http://dx.doi.org/10.1006/jcph.2001.6726.
[100] M. Muradoglu, S. Tasoglu, A front-tracking method for computational modeling of impact and spreading of viscous droplets on solid walls, Comput. Fluids 39 (2010) 615–625. http://dx.doi.org/10.1016/j.compfluid.2009.10.009.
[101] C.S. Peskin, Numerical analysis of blood flow in the heart, J. Comput. Phys. 25 (1977) 220–252. http://dx.doi.org/10.1016/0021-9991(77)90100-0.
[102] I. Donderwinkel, J.C.M. van Hest, N.R. Cameron, Bio-inks for 3D bioprinting: recent advances and future prospects, Polym. Chem. 8 (2017) 4451–4471. http://dx.doi.org/10.1039/C7PY00826K.
[103] D.B. Khismatullin, G.A. Truskey, Three-dimensional numerical simulation of receptor-mediated leukocyte adhesion to surfaces: effects of cell deformability and viscoelasticity, Phys. Fluids 17 (2005). http://dx.doi.org/10.1063/1.1862635.
[104] Z.Y. Luo, L. He, S.Q. Wang, S. Tasoglu, F. Xu, U. Demirci, B.F. Bai, Two-dimensional numerical study of flow dynamics of a nucleated cell tethered under shear flow, Chem. Eng. Sci. 119 (2014) 236–244. http://dx.doi.org/10.1016/j.ces.2014.07.048.
[105] C. Chung, J.M. Kim, M.A. Hulsen, K.H. Ahn, S.J. Lee, Effect of viscoelasticity on drop dynamics in 5:1:5 contraction/expansion microchannel flow, Chem. Eng. Sci. 64 (2009) 4515–4524. http://dx.doi.org/10.1016/j.ces.2009.05.049.
[106] C. Chung, J.M. Kim, K.H. Ahn, S.J. Lee, Numerical study on the effect of viscoelasticity on pressure drop and film thickness for a droplet flow in a confined microchannel, Korea Aust. Rheol. J. 21 (2009) 59–69. http://dx.doi.org/10.1016/j.jnnfm.2008.06.002.
[107] D. Izbassarov, M. Nooranidoost, S. Tasoglu, M. Muradoglu, Effects of viscoelasticity on droplet-based bioprinting, in: Proceedings of the 71st Annu. Meet. APS Div. Fluid Dyn., Atlanta, GA, 2018.
[108] K. Nair, M. Gandhi, S. Khalil, K.C. Yan, M. Marcolongo, K. Barbee, W. Sun, Characterization of cell viability during bioprinting processes, Biotechnol. J. 4 (2009) 1168–1177. http://dx.doi.org/10.1002/biot.200900004.
[109] S.E.D. Khalil, Deposition and structural formation of 3D alginate tissue scaffolds, 2005.
[110] T. Jungst, W. Smolan, K. Schacht, T. Scheibel, J. Groll, Strategies and molecular design criteria for 3D printable hydrogels, Chem. Rev. 116 (2016) 1496–1539. http://dx.doi.org/10.1021/acs.chemrev.5b00303.
[111] J. Malda, J. Visser, F.P. Melchels, T. Jüngst, W.E. Hennink, W.J.A. Dhert, J. Groll, D.W. Hutmacher, 25th anniversary article: engineering hydrogels for biofabrication, Adv. Mater. 25 (2013) 5011–5028. http://dx.doi.org/10.1002/adma.201302042.
[112] A. Ribeiro, M.M. Blokzijl, R. Levato, C.W. Visser, M. Castilho, W.E. Hennink, T. Vermonden, J. Malda, Assessing bioink shape fidelity to aid material development in 3D bioprinting, Biofabrication 10 (2018). http://dx.doi.org/10.1088/1758-5090/aa90e2.
[113] D. Therriault, S.R. White, J.A. Lewis, Rheological behavior of fugitive organic inks for direct-write assembly, Appl. Rheol. 17 (2007) 1–8.
[114] S. Di Risio, N. Yan, Piezoelectric ink-jet printing of horseradish peroxidase: effect of ink viscosity modifiers on activity, Macromol. Rapid Commun. 28 (2007) 1934–1940. http://dx.doi.org/10.1002/marc.200700226.
[115] C.J. Ferris, K.G. Gilmore, G.G. Wallace, M. In Het Panhuis, Biofabrication: an overview of the approaches used for printing of living cells, Appl. Microbiol. Biotechnol. 97 (2013) 4243–4258. http://dx.doi.org/10.1007/s00253-013-4853-6.
[116] R.E. Saunders, J.E. Gough, B. Derby, Delivery of human fibroblast cells by piezoelectric drop-on-demand inkjet printing, Biomaterials 29 (2008) 193–203. http://dx.doi.org/10.1016/j.biomaterials.2007.09.032.
[117] E. Li, E. Tan, S. Thoroddsen, Piezoelectric drop-on-demand inkjet printing of rat fibroblast cells: survivability study and pattern printing, arXiv Prepr. arXiv. arXiv:1310.0656, 2013, pp. 15–22. http://arxiv.org/abs/1310.0656.
[118] J. Tritz, R. Rahouadj, N. de Isla, N. Charif, A. Pinzano, D. Mainard, D. Bensoussan, P. Netter, J.-F. Stoltz, N. Benkirane-Jessel, C. Huselstein, Designing a three-dimensional alginate hydrogel by spraying method for cartilage tissue engineering, Soft Matter 6 (2010) 5165. http://dx.doi.org/10.1039/c000790k.
[119] C. Fredriksson, G. Kratz, F. Huss, Transplantation of cultured human keratinocytes in single cell suspension: a comparative in vitro study of different application techniques, Burns 34 (2008) 212–219. http://dx.doi.org/10.1016/j.burns.2007.03.008.
[120] Y. Nahmias, A. Arneja, T.T. Tower, M.J. Renn, D.J. Odde, Cell patterning on biological gels via cell spraying through a mask, Tissue Eng. 11 (2005) 701–708. http://dx.doi.org/10.1089/ten.2005.11.701.
[121] C. Clanet, C. Béguin, D. Richard, D. Quéré, Maximal deformation of an impacting drop, J. Fluid Mech. 517 (2004) 199–208. http://dx.doi.org/10.1017/S0022112004000904.
[122] C.W. Visser, Y. Tagawa, C. Sun, D. Lohse, Microdroplet impact at very high velocity, Soft Matter 8 (2012) 10732. http://dx.doi.org/10.1039/c2sm26323h.
[123] C.W. Visser, P.E. Frommhold, S. Wildeman, R. Mettin, D. Lohse, C. Sun, Dynamics of high-speed micro-drop impact: numerical simulations and experiments at frame-to-frame times below 100 ns, Soft Matter 11 (2015) 1708–1722. http://dx.doi.org/10.1039/C4SM02474E.
[124] T. Tran, H. De Maleprade, C. Sun, D. Lohse, Air entrainment during impact of droplets on liquid surfaces, J. Fluid Mech. 726 (2013) 1–11. http://dx.doi.org/10.1017/jfm.2013.261.
[125] A. Blaeser, D.F. Duarte Campos, U. Puster, W. Richtering, M.M. Stevens, H. Fischer, Controlling shear stress in 3D bioprinting is a key factor to balance printing resolution and stem cell integrity, Adv. Healthc. Mater. 5 (2016) 326–333. http://dx.doi.org/10.1002/adhm.201500677.
[126] C.M.F. Potter, K.H. Lao, L. Zeng, Q. Xu, Role of biomechanical forces in stem cell vascular lineage differentiation, Arterioscler. Thromb. Vasc. Biol. 34 (2014) 2184–2190. http://dx.doi.org/10.1161/ATVBAHA.114.303423.
[127] M.M. Stevens, R.P. Marini, D. Schaefer, J. Aronson, R. Langer, V.P. Shastri, In vivo engineering of organs: the bone bioreactor, Proc. Natl. Acad. Sci. USA 102 (2005) 11450–11455. http://dx.doi.org/10.1073/pnas.0504705102.
[128] M.S. Hahn, B.A. Teply, M.M. Stevens, S.M. Zeitels, R. Langer, Collagen composite hydrogels for vocal fold lamina propria restoration, Biomaterials 27 (2006) 1104–1109. http://dx.doi.org/10.1016/j.biomaterials.2005.07.022.
[129] G.L. Fillmore, Drop velocity from an ink-jet nozzle, IEEE Trans. Ind. Appl. IA-19 (1983) 1098–1103. http://dx.doi.org/10.1109/TIA.1983.4504341.
[130] A. van der Bos, M.-J. van der Meulen, T. Driessen, M. van den Berg, H. Reinten, H. Wijshoff, M. Versluis, D. Lohse, Velocity profile inside piezoacoustic inkjet droplets in flight: comparison between experiment and numerical simulation, Phys. Rev. Appl. 1 (2014) 14004.
[131] X. Yang, V. Mironov, Q. Wang, Modeling fusion of cellular aggregates in biofabrication using phase field theories, J. Theor. Biol. 303 (2012) 110–118. http://dx.doi.org/10.1016/j.jtbi.2012.03.003.
[132] Y. Sun, Q. Wang, Modeling and simulations of multicellular aggregate self-assembly in biofabrication using kinetic Monte Carlo methods, Soft Matter 9 (2013) 2172. http://dx.doi.org/10.1039/c2sm27090k.
[133] M.S. Steinberg, M.S. Steinberg, Reconstruction of tissues by dissociated cells, Science 141 (80) (1963) 401–408.
[134] R.A. Foty, M.S. Steinberg, The differential adhesion hypothesis: a direct evaluation, Dev. Biol. 278 (2005) 255–263. http://dx.doi.org/10.1016/j.ydbio.2004.11.012.
[135] J.M. Pérez-Pomares, R.A. Foty, Tissue fusion and cell sorting in embryonic development and disease: biomedical implications, BioEssays 28 (2006) 809–821. http://dx.doi.org/10.1002/bies.20442.
[136] K. Jakab, A. Neagu, V. Mironov, R.R. Markwald, G. Forgacs, Engineering biological structures of prescribed shape using self-assembling multicellular systems, Proc. Natl. Acad. Sci. USA 101 (2004) 2864–2869. http://dx.doi.org/10.1073/pnas.0400164101.
[137] A. Neagu, K. Jakab, R. Jamison, G. Forgacs, Role of physical mechanisms in biological self-organization, Phys. Rev. Lett. 95 (2005) 1–4. http://dx.doi.org/10.1103/PhysRevLett.95.178104.
[138] E. Flenner, F. Marga, A. Neagu, I. Kosztin, G. Forgacs, Relating biophysical properties across scales, Curr. Top. Dev. Biol. 81 (2008) 461–483. http://dx.doi.org/10.1016/S0070-2153(07)81016-7.
[139] F. Marga, A. Neagu, I. Kosztin, G. Forgacs, Developmental biology and tissue engineering, Birth Defects Res. Part C - Embryo Today Rev. 81 (2007) 320–328. http://dx.doi.org/10.1002/bdrc.20109.
[140] V. Mironov, R.P. Visconti, V. Kasyanov, G. Forgacs, C.J. Drake, R.R. Markwald, Organ printing: tissue spheroids as building blocks, Biomaterials 30 (2009) 2164–2174. http://dx.doi.org/10.1016/j.biomaterials.2008.12.084.
[141] J.L. Guermond, J. Shen, On the error estimates for the totational pressure-correction projection methods, Math. Comput. 73 (2003) 1719–1737. http://dx.doi.org/10.1090/S0025-5718-03-01621-1.